The Astrophysical Journal, 918:88 (19pp), 2021 September 10 https://doi.org/10.3847/1538-4357/ac0db8


# Resolved Dwarf Galaxy Searches within ∼5 Mpc with the Vera Rubin Observatory and Subaru Hyper Suprime-Cam*

Burçin Mutlu-Pakdil[1,2,12], David J. Sand[3], Denija Crnojević[4], Alex Drlica-Wagner[1,2,5], Nelson Caldwell[6], Puragra Guhathakurta[7], Anil C. Seth[8], Joshua D. Simon[9], Jay Strader[10], and Elisa Toloba[11]

[1] Kavli Institute for Cosmological Physics, University of Chicago, Chicago, IL 60637, USA; burcinmp@uchicago.edu
[2] Department of Astronomy and Astrophysics, University of Chicago, Chicago IL 60637, USA
[3] Steward Observatory, University of Arizona, 933 North Cherry Avenue, Tucson, AZ 85721, USA
[4] University of Tampa, 401 West Kennedy Boulevard, Tampa, FL 33606, USA
[5] Fermi National Accelerator Laboratory, P.O. Box 500, Batavia, IL 60510, USA
[6] Center for Astrophysics, Harvard & Smithsonian, 60 Garden Street, Cambridge, MA 02138, USA
[7] University of California Observatories/Lick Observatory, University of California, Santa Cruz, CA 95064, USA
[8] University of Utah, 115 South 1400 East, Salt Lake City, UT 84112-0830, USA
[9] Observatories of the Carnegie Institution for Science, 813 Santa Barbara Street, Pasadena, CA 91101, USA
[10] Department of Physics and Astronomy, Michigan State University, East Lansing, MI 48824, USA
[11] Department of Physics, University of the Pacific, 3601 Pacific Avenue, Stockton, CA 95211, USA
*Received 2021 May 4; revised 2021 June 14; accepted 2021 June 21; published 2021 September 15*

## Abstract

We present a preview of the faint dwarf galaxy discoveries that will be possible with the Vera C. Rubin Observatory and Subaru Hyper Suprime-Cam in the next decade. In this work, we combine deep ground-based images from the Panoramic Imaging Survey of Centaurus and Sculptor and extensive image simulations to investigate the recovery of faint, resolved dwarf galaxies in the Local Volume with a matched-filter technique. We adopt three fiducial distances (1.5, 3.5, and 5 Mpc) and quantitatively evaluate the effects on dwarf detection of varied stellar backgrounds, ellipticity, and Milky Way foreground contamination and extinction. We show that our matched-filter method is powerful for identifying both compact and extended systems, and near-future surveys will be able to probe at least ∼4.5 mag below the tip of the red giant branch (TRGB) for a distance of up to 1.5 Mpc and ∼2 mag below the TRGB at 5 Mpc. This will push the discovery frontier for resolved dwarf galaxies to fainter magnitudes, lower surface brightnesses, and larger distances. Our simulations show the secure census of dwarf galaxies down to $M_V \approx -5$, $-7$, and $-8$ will soon be within reach, out to 1.5, 3.5, and 5 Mpc, respectively, allowing us to quantify the statistical fluctuations in satellite abundances around hosts and parse environmental effects as a function of host properties.

*Unified Astronomy Thesaurus concepts:* Dwarf galaxies (416); Photometry (1234); Galaxies (573); Cosmology (343); Local Group (929)

## 1. Introduction

The Λ+cold dark matter (ΛCDM) model for structure formation is successful on large scales (≳10 Mpc) and provides a good match to the structure in the cosmic microwave background and the large-scale distribution of galaxies. In this model, galaxies grow hierarchically within dark matter halos (e.g., Springel et al. 2006), but quantitatively verifying this on small galaxies has met with challenges, particularly with respect to the faint end of the galaxy luminosity function (for a recent review, see Bullock & Boylan-Kolchin 2017). These challenges have been widely discussed in the literature and include the "missing satellites problem" (e.g., Klypin et al. 1999; Moore et al. 1999), "too big to fail" (e.g., Boylan-Kolchin et al. 2011, 2012), and the apparent planes of satellites around nearby galaxies (e.g., Pawlowski et al. 2012; Ibata et al. 2013; Müller et al. 2018).

Significant progress has been made in addressing these small-scale ΛCDM challenges on the theoretical front with the inclusion of realistic baryonic physics into galaxy-scale simulations (e.g., Brooks et al. 2013; Sawala et al. 2016; Wetzel et al. 2016; Samuel et al. 2021; Engler et al. 2021), which roughly match the properties of the Milky Way (MW) satellite system. Likewise, the number and diversity of satellites around the MW continues to expand (for instance, most recently, Mau et al. 2020; Cerny et al. 2021; see Simon 2019 for a recent review). The Local Group, and the MW in particular, will continue to be an important testing ground for understanding the astrophysics and cosmological implications of the very faintest dwarf galaxy satellites (e.g., Munshi et al. 2019; Nadler et al. 2021, among others).

Ultimately, to fully test the ΛCDM model and the important astrophysics relevant for the formation and evolution of dwarf galaxies (e.g., stellar and supernova feedback, reionization, tidal and ram pressure stripping, etc.), studies of faint satellite systems beyond the Local Group are necessary in order to sample primary halos with a range of masses, morphologies, and environments. Observationally, this work is now underway using wide-field imaging data sets centered around primary galaxies with a range of masses (e.g., Chiboucas et al. 2013; Crnojević et al. 2014; Sand et al. 2014, 2015a; Carlin et al. 2016; Crnojević et al. 2016; Toloba et al. 2016; Danieli et al. 2017; Smercina et al. 2018; Bennet et al. 2019; Crnojević et al. 2019; Bennet et al. 2020; Carlsten et al. 2021; Davis et al. 2021; Drlica-Wagner et al. 2021), as well as spectroscopic surveys around MW analogs at larger distances (Geha et al. 2017; Mao et al. 2021). Numerical studies are also addressing the scatter in

* This paper includes data gathered with the 6.5 m Magellan Telescope at Las Campanas Observatory, Chile.
[12] Corresponding author.

satellite properties seen in MW-like galaxies, as well as their physical origins (e.g., Font et al. 2021). Searches for faint galaxies in the field are also uncovering a multitude of dwarf galaxy systems using several techniques (e.g., Sand et al. 2015b; Tollerud et al. 2015; Bennet et al. 2017; Leisman et al. 2017; Bennet et al. 2018; Greco et al. 2018; Zaritsky et al. 2019; Tanoglidis et al. 2021, among many others).

In this work, we will investigate the prospects for identifying faint dwarf galaxies in the nearby universe ($D \lesssim 5$ Mpc) using resolved stellar populations with current and near-future ground-based instrumentation. Successful wide-field searches are already underway in this area of parameter space with at least four instruments: the Megacam imager on the Canada–France–Hawaii Telescope (CFHT; Boulade et al. 2003), the Megacam imager on the Magellan Clay telescope (McLeod et al. 2015), the Dark Energy Camera (DECam) on the Blanco telescope (Flaugher et al. 2015), and the Hyper Suprime-Cam (HSC) on the Subaru telescope (Miyazaki et al. 2018). This work will accelerate and expand to the entire southern sky with the advent of the Vera C. Rubin Observatory (Rubin) Legacy Survey of Space and Time (LSST). Also on the horizon is the Nancy Grace Roman Space Telescope, which will be an excellent platform for discovering resolved dwarf galaxies in the Local Volume (Akeson et al. 2019) and the subject of a future paper.

Here we combine image-level simulations of resolved, faint dwarf galaxies at varying distances, luminosities, ellipticities, and sizes with deep ground-based images from the Panoramic Imaging Survey of Centaurus and Sculptor (PISCeS; Crnojević et al. 2014; Sand et al. 2014; Crnojević et al. 2016; Toloba et al. 2016; Crnojević et al. 2019; Hughes et al. 2021). As we discuss, these data are of nearly the same quality and depth as those expected from the 10 yr LSST and can be used to rigorously quantify the detectability of faint dwarf galaxies in the Local Volume using state-of-the-art techniques. By comparing these recovery statistics with the sample of known nearby galaxy hosts (see Table 1 and Figure 1), we can forecast the ensemble of dwarf luminosity functions that will be uncovered in the LSST (and HSC) era. First, in Section 2, we present the landscape of resolved dwarf studies. In Section 3, we describe our methodology for creating mock observations of resolved, faint dwarf galaxies (Section 3.1) and introduce the matched-filter technique as a powerful tool to search both compact and extended systems (Section 3.2). In Section 4, we present the results of our experiments, providing our recovery fraction as a function of the dwarf parameters. In Section 5, we discuss our results and provide a preview of faint dwarf galaxy discoveries that will be possible in the LSST (and HSC) era. Finally, we summarize our key results in Section 6.

## 2. The Landscape for Resolved Dwarf Studies

For most of this work, we focus on the identification of faint dwarf galaxies with predominantly old, metal-poor stellar populations within roughly the virial radius of larger host galaxies. We focus on the luminosity range ($M_V \gtrsim -11$ mag), where the Updated Nearby Galaxy Catalog (Karachentsev et al. 2013) suggests that incompleteness becomes significant in the existing sample of galaxies. In this luminosity range, most dwarf satellites around more massive hosts have been quenched and stripped of their gas (e.g., Spekkens et al. 2014; Karunakaran et al. 2020; Putman et al. 2021, Karunakaran et al. 2021) and thus do not have younger stellar populations (exceptions include Antlia and Antlia B, likely satellites of NGC 3109). It is worth pointing out that even gas-rich dwarfs have a majority of their mass formed at old ages (e.g., Weisz et al. 2011) and thus would be detectable using methods that just focus on the detectability of old stars. Furthermore, any dwarf with a younger stellar population will be easier to detect due to the presence of relatively rare blue stars, so the presentation in this work can be considered conservative. The discovery space for faint dwarf galaxies in the field, with typically younger stellar populations on average, will be broader than that presented here.

To gauge the distance range that we can identify and study faint dwarf galaxies in resolved stars, we plot the color–magnitude diagram (CMD) of the MW satellite Draco ($M_V = -8.7$ mag; $\sim 2.5 \times 10^5$ $L_\odot$; Martin et al. 2008) in Figure 2, using data from the Sloan Digital Sky Survey (SDSS; Ahumada et al. 2020). Draco is a faint member of the MW's "classical" satellites, which were discovered prior to the era of digital sky surveys, and its CMD is typical; it displays a clear red giant branch (RGB) due to an old, metal-poor stellar population, as well as a prominent horizontal branch (HB). In Figure 2, we also mark the position of the tip of the red giant branch (TRGB) in the $r$ band, as determined from theoretical isochrones ($M_r = -3.0$ mag; Sand et al. 2014).

Current and planned deep-imaging surveys around nearby galaxies will ultimately have different faint-end magnitude limits, although they will typically reach $r \approx 27$th mag or fainter. LSST expects a $5\sigma$ point-source image depth of ($g$, $r$, $i$) = (27.4, 27.5, 26.8) mag after the 10 yr survey (Ivezić et al. 2019). Meanwhile, current resolved dwarf search programs with HSC reach a 50% completeness limit of ($g$, $i$) = (27.5, 26.7) mag (e.g., Carlin et al. 2019), although even deeper depths are possible with longer exposure times in good conditions (e.g., Tanaka et al. 2017; Müller et al. 2019). Here we will use the best image quality fields of the PISCeS program, which searches for resolved dwarfs and other halo substructures around NGC 253 and Cen A with the Magellan Megacam, with corresponding 50% completeness limits of ($g$, $r$) = (27.83, 27.35) and (27.51, 27.01) mag, respectively, at a signal-to-noise ratio detection threshold of three. These limits include stringent cuts made to select point sources, as we describe below, and are thus difficult to encapsulate with simple metrics. These same fields have a final image FWHM of ($g$, $r$) = (0.″5, 0.″6) and (0.″5, 0.″5), respectively. By using data in both Cen A ($b = 19°$) and NGC 253 ($b = -88°$), we can examine the effects of MW foreground contamination on dwarf detection (see Section 4.4).

Adopting the deep limits from the PISCeS program fields, we mark the corresponding depths at three fiducial distances, $D = 1.5$, 3.5, and 5 Mpc, on the Draco CMD in Figure 2. Current and next-generation deep surveys will be able to probe $\sim$2 mag below the TRGB at 5 Mpc and correspondingly deeper for closer distances, clearly making resolved stellar searches for faint satellites (and other substructures) feasible. Resolved dwarf searches beyond $\sim$5 Mpc will likely have diminishing returns, although they should be pursued through other venues, such as the Roman Space Telescope (Akeson et al. 2019).

To put this in context with the Local Volume, we compile a list of nearby galaxies ($D \lesssim 5$ Mpc) around which faint satellite galaxies could be found (see Table 1, taken from the Updated Nearby Galaxy Catalog; Karachentsev et al. 2013). This list is divided into three categories based on the $K$-band luminosities:

**Table 1**
Prominent Galaxies within ≈5 Mpc

| Galaxy | R.A. (deg) | Decl. (deg) | $l$ (deg) | $b$ (deg) | Dist. (Mpc) | $\log(L_K)$ ($L_\odot$) | $\log(M_{\rm halo})$ ($M_\odot$) | $R_{\rm vir}$ (kpc) | $A_V$ (mag) | $V_{\rm LG}$ (km s$^{-1}$) | $\Theta_5$ | Morph. |
|---|---|---|---|---|---|---|---|---|---|---|---|---|
| (1) | (2) | (3) | (4) | (5) | (6) | (7) | (8) | (9) | (10) | (11) | (12) | (13) |
| MW Luminosity Group ($\log(L_K/L_\odot) \gtrsim 10$) | | | | | | | | | | | | |
| MW | 266.417 | −29.0078 | ⋯ | ⋯ | 0.01 | 10.78 | 12.34 | 260 | ⋯ | −65 | 2.9 | Sp |
| M31 | 10.685 | 41.2692 | 121.1744 | −21.5729 | 0.77 | 10.73 | 12.28 | 250 | 0.17 | −29 | 3.2 | Sp |
| IC 342 | 56.704 | 68.0958 | 138.1724 | 10.5801 | 3.28 | 10.60 | 12.13 | 220 | 1.53 | 244 | 0.3 | Sp |
| NGC 4945 | 196.359 | −49.4711 | 305.2721 | 13.3399 | 3.47 | 10.66 | 12.20 | 299. | 0.48 | 299 | 0.9 | Sp |
| M82 | 148.975 | 69.6825 | 141.4048 | 40.5671 | 3.61 | 10.59 | 12.10 | 220 | 0.43 | 328 | 3.1 | Sp |
| Cen A | 201.370 | −43.0167 | 309.5159 | 19.4173 | 3.68 | 10.89 | 12.50 | 300 | 0.32 | 310 | 1.6 | S0 |
| NGC 253 | 11.893 | −25.2922 | 97.3692 | −87.9640 | 3.70 | 10.98 | 12.64 | 330 | 0.05 | 276 | 0.2 | Sp |
| M81 | 148.890 | 69.0667 | 142.0900 | 40.8997 | 3.70 | 10.93 | 12.56 | 310 | 0.22 | 104 | 2.8 | Sp |
| Circinus | 213.289 | −65.3392 | 311.3260 | −3.8080 | 4.20 | 10.60 | 12.13 | 220 | 3.99 | 189 | −0.4 | Sp |
| M94 | 192.723 | 41.1194 | 123.3631 | 76.0074 | 4.41 | 10.61 | 12.14 | 230 | 0.05 | 352 | 0.1 | Sp |
| M64 | 194.184 | 21.6847 | 315.6803 | 84.4233 | 4.41 | 10.48 | 12.01 | 200 | 0.11 | 365 | −0.7 | Sp |
| M83 | 204.250 | −29.8678 | 314.5838 | 31.9730 | 4.90 | 10.86 | 12.45 | 290 | 0.18 | 307 | 0.8 | Sp |
| LMC Analogs ($9 \lesssim \log(L_K/L_\odot) \lesssim 10$) | | | | | | | | | | | | |
| LMC | 80.894 | −69.7561 | 280.4652 | −32.8884 | 0.05 | 9.42 | 11.29 | 120 | 0.21 | 28 | 3.6 | Sp |
| M33 | 23.462 | 30.6603 | 133.6098 | −31.3306 | 0.93 | 9.62 | 11.40 | 130 | 0.11 | 34 | 1.5 | Sp |
| NGC 300 | 13.723 | −37.6825 | 299.2075 | −79.4208 | 2.09 | 9.41 | 11.28 | 120 | 0.04 | 116 | 0.2 | Sp |
| NGC 55 | 3.785 | −39.2203 | 332.6670 | −75.7390 | 2.11 | 9.48 | 11.32 | 120 | 0.04 | 111 | 0.2 | Sp |
| NGC 404 | 17.362 | 35.7175 | 127.0345 | −27.0107 | 2.98 | 9.26 | 11.21 | 110 | 0.16 | 193 | −0.7 | S0 |
| UGCA 86 | 59.956 | 67.1253 | 139.7729 | 10.6385 | 2.98 | 9.13 | 11.15 | 110 | 2.57 | 280 | 1.2 | Sp |
| NGC 1569 | 67.705 | 64.8481 | 143.6821 | 11.2418 | 3.19 | 9.40 | 11.28 | 120 | 1.90 | 106 | 1.2 | Sp |
| NGC 2403 | 114.214 | 65.5994 | 150.5691 | 29.1859 | 3.19 | 9.86 | 11.53 | 140 | 0.11 | 262 | 0.6 | Sp |
| ESO 383-87 | 207.328 | −36.0614 | 315.8471 | 25.3547 | 3.19 | 9.05 | 11.11 | 100 | 0.20 | 108 | 0.6 | Sp |
| UGCA 105 | 78.563 | 62.5808 | 148.5216 | 13.6581 | 3.39 | 9.14 | 11.15 | 110 | 0.86 | 281 | 0.4 | Sp |
| NGC 5253 | 204.983 | −31.6400 | 314.8596 | 30.1061 | 3.44 | 9.08 | 11.13 | 100 | 0.15 | 193 | 0.5 | Sp |
| Holm II | 124.767 | 70.7142 | 144.2839 | 32.6882 | 3.47 | 9.20 | 11.18 | 110 | 0.09 | 311 | 1.0 | Sp |
| NGC 7793 | 359.456 | −32.5900 | 4.5224 | −77.1704 | 3.63 | 9.70 | 11.44 | 130 | 0.05 | 250 | 0.3 | Sp |
| NGC 2976 | 146.815 | 67.9136 | 143.9174 | 40.9042 | 3.66 | 9.44 | 11.30 | 120 | 0.20 | 142 | 3.1 | Sp |
| NGC 5102 | 200.491 | −36.6297 | 309.7323 | 25.8386 | 3.66 | 9.70 | 11.44 | 130 | 0.15 | 227 | 1.1 | Sp |
| NGC 247 | 11.785 | −20.7600 | 113.9392 | −83.5565 | 3.72 | 9.50 | 11.33 | 120 | 0.05 | 216 | 1.6 | Sp |
| NGC 3077 | 150.838 | 68.7339 | 141.8973 | 41.6622 | 3.85 | 9.57 | 11.36 | 120 | 0.18 | 159 | 2.4 | Sp |
| IC 2574 | 157.093 | 68.4161 | 140.2045 | 43.6032 | 3.93 | 9.33 | 11.24 | 110 | 0.10 | 183 | 1.7 | Sp |
| NGC 4449 | 187.047 | 44.0944 | 136.8514 | 72.4000 | 4.27 | 9.68 | 11.42 | 130 | 0.05 | 249 | 0.8 | Sp |
| NGC 1313 | 49.564 | −66.4975 | 283.3589 | −44.6443 | 4.31 | 9.57 | 11.36 | 120 | 0.30 | 264 | −0.6 | Sp |
| NGC 4244 | 184.375 | 37.8075 | 154.5637 | 77.1572 | 4.31 | 9.52 | 11.34 | 120 | 0.06 | 259 | 0.5 | Sp |
| NGC 4236 | 184.180 | 69.4656 | 127.4135 | 47.3595 | 4.41 | 9.61 | 11.39 | 130 | 0.04 | 157 | 0.0 | Sp |
| NGC 4395 | 186.458 | 33.5461 | 162.0819 | 81.5356 | 4.76 | 9.47 | 11.31 | 120 | 0.05 | 308 | 0.1 | Sp |
| SMC Analogs ($8.0 \lesssim \log(L_K/L_\odot) \lesssim 9.0$) | | | | | | | | | | | | |
| SMC | 13.158 | −72.8003 | 302.8084 | −44.3277 | 0.06 | 8.85 | 11.03 | 100 | 0.10 | −22. | 3.6 | Sp |
| M32 | 10.675 | 40.8664 | 121.1510 | −21.9751 | 0.79 | 9.09 | 11.13 | 100 | 0.17 | 64 | 4.7 | S0 |
| NGC 6822 | 296.240 | −14.8031 | 25.3398 | −18.3989 | 0.52 | 8.38 | 10.85 | 80 | 0.65 | 64 | 0.6 | Irr |
| NGC 185 | 9.742 | 48.3361 | 120.7918 | −14.4838 | 0.66 | 8.36 | 10.84 | 80 | 0.51 | 73 | 2.3 | S0 |
| NGC 147 | 8.298 | 48.5078 | 119.8158 | −14.2536 | 0.76 | 8.21 | 10.79 | 80 | 0.47 | 85 | 2.8 | S0 |
| IC 1613 | 16.199 | 2.1333 | 129.7344 | −60.5619 | 0.76 | 8.10 | 10.75 | 80 | 0.07 | −89 | 0.8 | Irr |
| IC 10 | 5.102 | 59.2917 | 118.9727 | −3.3413 | 0.79 | 8.63 | 10.94 | 90 | 4.30 | −62 | 1.6 | Irr |
| NGC 205 | 10.094 | 41.6864 | 120.7178 | −21.1378 | 0.80 | 8.90 | 11.05 | 100 | 0.17 | 47 | 4.4 | S0 |
| NGC 3109 | 150.780 | −26.1600 | 262.1029 | 23.0706 | 1.34 | 8.58 | 10.92 | 90 | 0.18 | 110 | −0.1 | Sp |
| IC 5152 | 330.675 | −51.2953 | 343.9201 | −50.1932 | 1.96 | 8.71 | 10.97 | 90 | 0.07 | 73 | −0.6 | Sp |
| IC 3104 | 184.692 | −79.7261 | 301.4140 | −16.9508 | 2.36 | 8.41 | 10.86 | 80 | 1.12 | 170 | −0.6 | Sp |
| IC 4662 | 266.776 | −64.6403 | 328.5479 | −17.8450 | 2.55 | 8.72 | 10.98 | 90 | 0.19 | 139 | −0.7 | Sp |
| DDO 125 | 186.924 | 43.4939 | 137.7510 | 72.9447 | 2.61 | 8.06 | 10.74 | 80 | 0.06 | 251 | −0.4 | Sp |
| ESO 274-001 | 228.556 | −46.8125 | 326.8040 | 9.3341 | 2.79 | 8.92 | 11.06 | 100 | 0.69 | 337 | −0.2 | Sp |
| NGC 4214 | 183.912 | 36.3275 | 160.2556 | 78.0735 | 2.88 | 8.98 | 11.08 | 100 | 0.06 | 295 | 0.8 | Sp |
| NGC 1560 | 68.2079 | 71.8811 | 138.3682 | 16.0217 | 2.99 | 8.60 | 10.93 | 90 | 0.51 | 170 | 0.9 | Sp |
| NGC 5206 | 203.433 | −48.1511 | 310.1842 | 14.1242 | 3.21 | 8.95 | 11.07 | 100 | 0.33 | 334 | 1.1 | S0 |
| UGCA 092 | 68.001 | 63.6139 | 144.7030 | 10.5106 | 3.22 | 8.04 | 10.74 | 80 | 2.15 | 93 | 1.9 | Irr |
| NGC 2366 | 112.228 | 69.2053 | 146.4304 | 28.5360 | 3.28 | 8.70 | 10.97 | 90 | 0.10 | 251 | 1.0 | Irr |
| NGC 5237 | 204.412 | −42.8475 | 311.8775 | 19.2202 | 3.33 | 8.43 | 10.87 | 90 | 0.27 | 122 | 1.3 | Sp |

**Table 1**
(Continued)

| Galaxy | R.A. (deg) | Decl. (deg) | $l$ (deg) | $b$ (deg) | Dist. (Mpc) | $\log(L_K)$ ($L_\odot$) | $\log(M_{\rm halo})$ ($M_\odot$) | $R_{\rm vir}$ (kpc) | $A_V$ (mag) | $V_{\rm LG}$ (km s$^{-1}$) | $\Theta_5$ | Morph. |
|---|---|---|---|---|---|---|---|---|---|---|---|---|
| (1) | (2) | (3) | (4) | (5) | (6) | (7) | (8) | (9) | (10) | (11) | (12) | (13) |
| KDG 61 | 149.261 | 68.5917 | 142.5023 | 41.2832 | 3.66 | 8.11 | 10.76 | 80 | 0.20 | 360 | 4.0 | S0 |
| ESO 269-58 | 197.637 | −46.9908 | 306.3161 | 15.7553 | 3.75 | 8.86 | 11.03 | 100 | 0.30 | 140 | 1.6 | Sp |
| ESO 269-66 | 198.288 | −44.8900 | 306.9690 | 17.8115 | 3.75 | 8.42 | 10.87 | 90 | 0.26 | 528 | 2.1 | S0 |
| ESO 324-024 | 201.906 | −41.4806 | 310.1749 | 20.8817 | 3.78 | 8.35 | 10.84 | 80 | 0.31 | 272 | 2.4 | Sp |
| KK 197 | 200.507 | −42.5356 | 308.9215 | 19.9801 | 3.84 | 8.11 | 10.76 | 80 | 0.47 | 388 | 2.4 | S0 |
| DDO 82 | 157.646 | 70.6194 | 137.8957 | 42.1780 | 3.93 | 8.39 | 10.85 | 80 | 0.11 | 207 | 1.7 | Sp |
| NGC 625 | 23.7708 | −41.4364 | 273.6742 | −73.1206 | 4.02 | 8.96 | 11.07 | 100 | 0.05 | 325 | −0.3 | Sp |
| Holm I | 145.135 | 71.1864 | 140.7250 | 38.6596 | 4.02 | 8.05 | 10.74 | 80 | 0.14 | 291 | 1.5 | Irr |
| LV J1228+4358 | 187.187 | 43.9717 | 136.6518 | 72.5471 | 4.07 | 8.53 | 10.90 | 90 | 0.05 | 273 | 1.0 | Irr |
| DDO 168 | 198.619 | 45.9194 | 110.7617 | 70.6605 | 4.25 | 8.13 | 10.77 | 80 | 0.04 | 270 | 0.9 | Irr |
| NGC 2915 | 141.548 | −76.6264 | 291.9661 | −18.3573 | 4.29 | 8.74 | 10.98 | 90 | 0.75 | 191 | −0.8 | Sp |
| ESO 219-010 | 194.040 | −50.1439 | 303.7075 | 12.7207 | 4.29 | 8.03 | 10.73 | 80 | 0.61 | ⋯ | 0.4 | S0 |
| IC 4182 | 196.455 | 37.6058 | 107.7064 | 79.0937 | 4.35 | 8.70 | 10.97 | 90 | 0.04 | 357 | 1.0 | Sp |
| IC 4316 | 205.075 | −28.8944 | 315.6592 | 32.7668 | 4.35 | 8.21 | 10.80 | 80 | 0.15 | 369 | 0.7 | Irr |
| UGCA 442 | 355.942 | −31.9592 | 10.6915 | −74.5299 | 4.37 | 8.03 | 10.73 | 80 | 0.05 | 300 | −0.2 | Sp |
| NGC 4068 | 181.010 | 52.5886 | 138.9065 | 63.0448 | 4.39 | 8.30 | 10.82 | 80 | 0.06 | 290 | −0.1 | Sp |
| NGC 5238 | 203.678 | 51.6139 | 107.4046 | 64.1900 | 4.51 | 8.02 | 10.73 | 80 | 0.03 | 342 | −0.2 | Irr |
| ESO 245-005 | 26.2650 | −43.5981 | 273.0762 | −70.2894 | 4.57 | 8.53 | 10.91 | 90 | 0.05 | 307 | −0.6 | Sp |
| IC 3687 | 190.563 | 38.5019 | 131.9545 | 78.4649 | 4.57 | 8.19 | 10.79 | 80 | 0.06 | 377 | 1.2 | Irr |
| NGC 5204 | 202.402 | 58.4178 | 113.5007 | 58.0061 | 4.59 | 8.84 | 11.03 | 100 | 0.03 | 339 | −0.4 | Sp |
| ESO 059-001 | 112.830 | −68.1861 | 279.7732 | −21.4735 | 4.63 | 8.17 | 10.78 | 80 | 0.40 | 247 | −1.1 | Sp |
| NGC 5264 | 205.404 | −29.9139 | 315.7172 | 31.7090 | 4.79 | 8.88 | 11.04 | 100 | 0.14 | 269 | 2.5 | Sp |
| DDO 165 | 196.612 | 67.7042 | 120.7473 | 49.3604 | 4.83 | 8.23 | 10.80 | 80 | 0.07 | 196 | −0.2 | Sp |
| DDO 133 | 188.221 | 31.5392 | 164.3313 | 84.0174 | 4.88 | 8.24 | 10.80 | 80 | 0.04 | 320 | 0.5 | Irr |
| NGC 59 | 3.8546 | −21.4439 | 65.7125 | −80.0215 | 4.90 | 8.66 | 10.95 | 90 | 0.06 | 431 | −0.3 | S0 |
| DDO 126 | 186.771 | 37.1425 | 148.5971 | 78.7435 | 4.97 | 8.09 | 10.75 | 80 | 0.04 | 230 | 0.3 | Irr |

**Note.** Column 1: galaxy name. Column 2: R.A. (J2000.0). Column 3: decl. (J2000.0). Column 4: galactic longitude. Column 5: galactic latitude. Column 6: distance to the galaxy in megaparsecs. Column 7: logarithm of the *Ks*-band luminosity of the galaxy in solar units. Column 8: logarithm of the total halo mass in solar units, estimated from the $M_\star$–$M_{\rm halo}$ relation of Moster et al. (2010). Stellar masses are derived from the *K*-band luminosity by assuming a *K*-band mass-to-light ratio of unity. Column 9: virial radius in kiloparsecs, based on the Bryan & Norman (1998) definition, which is the radius such that the mean enclosed halo density is 104 times the critical density of the universe. Column 10: galactic extinction taken from NED. Column 11: radial velocity, in kilometers per second, of the galaxy relative to the Local Group centroid. Column 12: tidal index or density contrast, determined by the five most important neighbors. It serves as a proxy to the galaxy environment. Column 13: HEASARC Browse object classification of the galaxy based on the value of the morphological T type of the galaxy (i.e., Sp for spiral, S0 for lenticular, and Irr for irregular). The data are taken from the Updated Nearby Galaxy Catalog (Karachentsev et al. 2013; https://www.sao.ru/lv/lvgdb/) unless stated otherwise.

the MW luminosity group ($\log(L_K/L_\odot) \gtrsim 10$), Large Magellanic Cloud (LMC) analogs ($9 \lesssim \log(L_K/L_\odot) \lesssim 10$), and Small Magellanic Cloud (SMC) analogs ($8.0 \lesssim \log(L_K/L_\odot) \lesssim 9.0$). Similarly, we plot a collection of nearby galaxies in supergalactic coordinates in Figure 1, where we also demarcate the $D = 1.5$, 3.5, and 5 Mpc fiducial distances we consider in this work. For each galaxy in Table 1, we also note their Galactic coordinates and extinction in the $V$ band ($A_V$) as determined from the Schlafly & Finkbeiner (2011) calibration of the Schlegel et al. (1998) dust maps. Both extinction and foreground MW star counts may strongly affect prospects for Local Volume dwarf discovery (see Section 4.4). In addition, we derive their stellar masses ($M_\star$) from the *K*-band luminosity by assuming a *K*-band mass-to-light ratio of unity and then infer the total halo mass of each galaxy by using the $M_\star$–$M_{\rm halo}$ relationship given by Moster et al. (2010), along with the corresponding virial radius based on the Bryan & Norman (1998) definition (i.e., the radius such that the mean enclosed halo density is 104 times the critical density of the universe, $\rho_c = 3H_0^2/8\pi G$). Finally, we also include the tidal index parameter (see Karachentsev et al. 2013) for each galaxy in Table 1 as an indicator of local environment or density contrast. Recent work has indicated a tentative relationship between satellite richness and environment (Bennet et al. 2019), and future Local Volume surveys are required to investigate this further.

## 3. Methods

In this section, we describe our methodology for implanting simulated dwarf galaxies directly into our chosen PISCeS deep imaging fields as a proxy for similarly deep imaging surveys that may be performed with Rubin, HSC, or similar facilities. We implant dwarfs with a variety of luminosities, sizes, ellipticities, and surface brightnesses broadly consistent with the dwarf galaxy population identified in the Local Group. We focus on three different fiducial distances—1.5, 3.5, and 5 Mpc—to study these resolved, simulated dwarfs. Within a given region of sky, we also place dwarfs in different spatial positions to sample the effects that varied stellar backgrounds may have on dwarf detection. Additionally, we place a subset of dwarfs into our low Galactic latitude "Cen A" data to understand the effects of MW foreground contamination and extinction. We detect this simulated dwarf ensemble with a matched-filter technique to understand our recovery fraction as a function of the dwarf parameters described above.

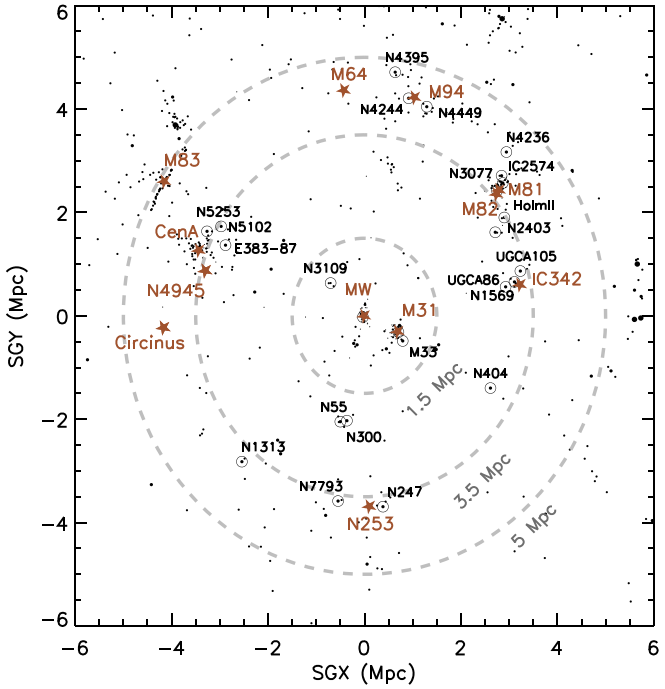


**Figure 1.** Nearby galaxies from the Updated Nearby Galaxy Catalog of Karachentsev et al. (2013) in a supergalactic coordinate projection. Brown stars correspond to galaxies with $\log(L_K/L_\odot) \gtrsim 10$, while other marked, prominent galaxies are less luminous (see Table 1). In this work, we explore the discovery space at three fiducial distances of 1.5, 3.5, and 5 Mpc, which encompass the major structures amenable to ground-based resolved star searches for dwarf galaxies.

### 3.1. Imaging Data and Mock Dwarf Observations

As mentioned earlier, we utilize the imaging data from the PISCeS survey, in which the halos of Cen A and NGC 253 have been targeted with the Megacam imager on the Magellan Clay 6.5 m telescope (McLeod et al. 2015) out to a projected radius of ∼150 kpc. Megacam has an $\sim 24' \times 24'$ field of view and a binned pixel scale of $0\farcs16$, similar to HSC ($0\farcs17$) and Rubin ($0\farcs2$). Our chosen NGC 253 deep imaging field was observed for $8 \times 300$ s in $g$ and $7 \times 300$ s in $r$, and the Cen A field was observed for $6 \times 300$ s in each of the $g$ and $r$ bands. The data were reduced in a standard way by the Smithsonian Astrophysical Observatory Telescope Data Center (see Crnojević et al. 2016 for further details on our survey strategy and observational methods). In this paper, we mostly use the best image quality field of NGC 253, which is 90% complete at $(g, r) = (26.98, 26.35)$ mag and 50% complete at $(g, r) = (27.83, 27.35)$ mag, as assessed by artificial star tests (see below). We make use of the deepest Cen A pointing (90% complete at $(g, r) = (26.53, 26.04)$ mag, 50% complete at $(g, r) = (27.51, 27.01)$ mag) to assess the effects of MW disk contamination in detecting dwarf galaxies (see Section 4.4). Both fields are approximately $R \sim 100$ kpc distant in projection from NGC 253 and Cen A, so halo contamination is negligible.

We assume that the stellar populations of the dwarf galaxies we wish to investigate are mainly composed of old, metal-poor stars and therefore well described by a single population. We construct our model galaxies by sampling from a 10 Gyr old stellar population with an overall metallicity of $[\mathrm{Fe/H}] = -2.0$ (using a Dartmouth isochrone; Dotter et al. 2008), assuming a Salpeter initial mass function. The stellar profiles of the dwarfs

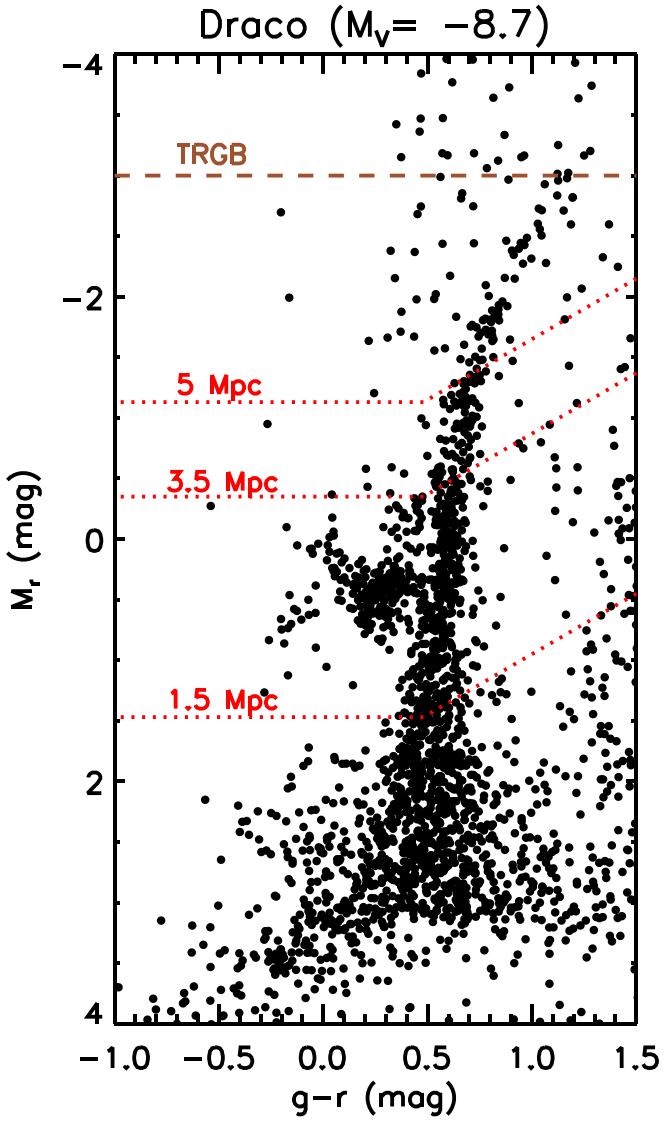


**Figure 2.** The CMD of the Draco dwarf spheroidal galaxy ($M_V = -8.7$ mag; $\sim 2.5 \times 10^5$ $L_\odot$) from the SDSS, plotted in absolute magnitude space. The approximate TRGB magnitude in the $r$ band is plotted at $M_r = -3.0$ mag (Sand et al. 2014). Assuming a 50% completeness magnitude of $(g, r) = (27.83, 27.35)$ mag, we have also plotted the corresponding absolute magnitude at our fiducial distances of $D = 1.5$, 3.5, and 5 Mpc. For dwarfs at $D \approx 5$ Mpc, one should be able to resolve stars ∼2 mag below the TRGB. Meanwhile, at $D \approx 1.5$ Mpc, HB stars should be resolved.

are generally well described by a single exponential model (e.g., Martin et al. 2008; Muñoz et al. 2018). We use an exponential profile with elliptical half-light radii ($r_h$) ranging from 0.02 to 5 kpc and corresponding ellipticities[13] of $\epsilon = [0, 0.3, 0.5]$. We intentionally focus on generating simulated galaxies that bracket the observed central surface brightness range of nearby dwarfs (e.g., by examining plots of $M_V$ versus $r_h$ for Local Group and Local Volume dwarf spheroidals and ultrafaints). As we expect to resolve HB stars at a distance of 1.5 Mpc (see Figure 2), we use a PARSEC isochrone (age = 10 Gyr, $[\mathrm{Fe/H}] = -2.0$; Bressan et al. 2012) for our simulations and include HB stars at this distance. Our pipeline then adds Galactic extinction to the stars on a source-by-source

[13] The ellipticity is defined as $\epsilon = 1 - b/a$, where $b$ is the scale length of the system along its minor axis and $a$ is that along its major axis.

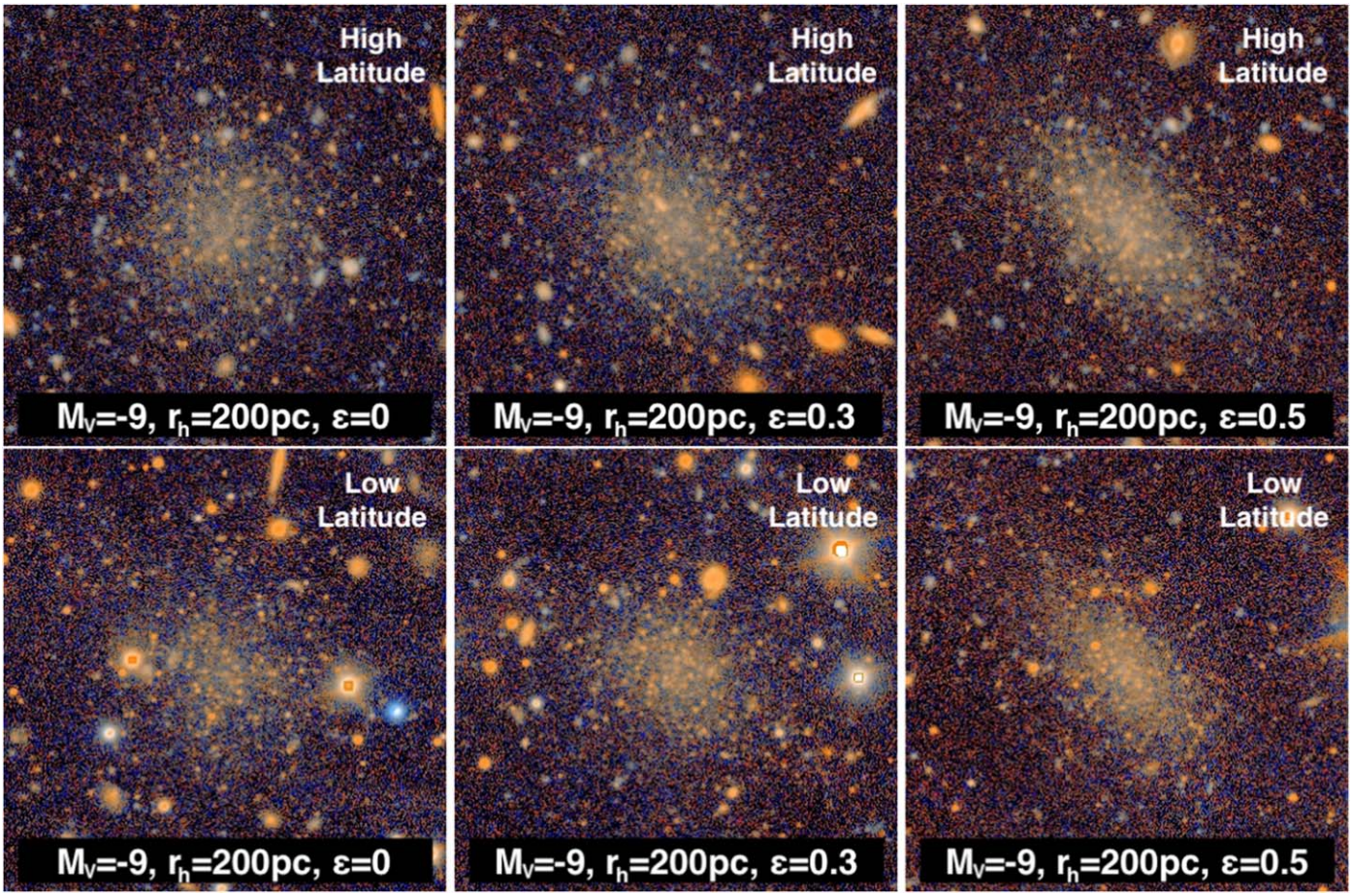


**Figure 3.** False-color images of simulated resolved dwarfs with $M_V = -9$ at 3.5 Mpc, with increasing ellipticities from left ($\epsilon = 0$) to right ($\epsilon = 0.5$). For each image, the size is $1' \times 1'$. In the top and bottom rows, dwarfs are placed in different sky positions in the NGC 253 and Cen A data, respectively. Note that NGC 253 is located at high Galactic latitude ($b = -88°$), such that the foreground extinction is very low ($E(B-V) = 0.02$ mag), while Cen A is located at low Galactic latitude with higher extinction ($b = 19°$, $E(B-V) = 0.12$ mag). We utilize the Cen A data to assess the effects of MW disk contamination and extinction in detecting dwarf galaxies.

basis by interpolating the Schlegel et al. (1998) extinction maps and the Schlafly & Finkbeiner (2011) correction coefficients and then injects these stars into the Megacam images with the DAOPHOT routine ADDSTAR (Stetson 1987, 1994). Based on the luminosity function, ∼85%–95% of the galaxy's light comes from stars of $r \lesssim 34.0$ mag; therefore, we choose to include stars with a magnitude of $r \lesssim 34.0$ mag for each galaxy realization. We experiment with 1 mag brighter and fainter cuts and find that our choice does not change the results. Overall, we simulate dwarfs with absolute magnitudes in the range $-11$ mag $\lesssim M_V \lesssim -4$ mag, dependent on the distance being examined, in order to understand the potential for dwarf galaxy detection over a broad range of luminosity.

For each luminosity and size bin, we simulate three different shapes ($\epsilon = [0, 0.3, 0.5]$) and place each simulated galaxy at five different positions in the field, resulting in 15 simulated systems. Figure 3 shows example simulated galaxies with three different ellipticities, which are placed in different sky positions in the NGC 253/Cen A fields (top/bottom). Because of implantation of stars well below the detection limits of the image, these dwarfs also include unresolved light. By performing multiple simulations for each size/luminosity bin, we account for "CMD shot noise" (Martin et al. 2008). A total of 2815 galaxies are generated in this manner. Our simulations are summarized in Table 2.

We treat the images with simulated dwarf galaxies in the same way as the unaltered images and perform point-spread function photometry using the DAOPHOT and ALLFRAME software suite (Stetson 1987, 1994), following the same methodology described in Crnojević et al. (2016), with small adjustments. We remove objects that are not point sources by culling our catalogs of outliers in $\chi^2$ versus magnitude, magnitude error versus magnitude, and sharpness versus magnitude space.[14] Instrumental magnitudes are then calibrated to the DES DR1 catalog (Abbott et al. 2018) for the NGC 253 field and the SDSS system for the Cen A field (Crnojević et al. 2016). The final calibrated catalogs are dereddened on a star-by-star basis using the Schlegel et al. (1998) reddening maps with the coefficients from Schlafly & Finkbeiner (2011). In Figures 4–6, we display example simulated galaxies for each fiducial distance along with their observed CMDs.

Before moving forward, we perform additional tests on a subset of our simulations for verification and validation of our pipeline. First, we fit an exponential profile to the two-dimensional distribution of stars consistent with each simulated dwarf by using the maximum-likelihood technique of Martin et al. (2008) as implemented by Sand et al. (2009). We

[14] We use a constant+exponential function for each of the photometric uncertainty, sharp, and $\chi^2$ as a function of magnitude.

**Table 2**
A Summary of Our Simulations

| $D$ (Mpc) (1) | $M_V$ (mag) (2) | $r_h$ (pc) (3) | Ellipticity (4) | $N_{\rm dwarf}$ (5) | Detectability (%) (6) | LG Analog (7) |
|---|---|---|---|---|---|---|
| 1.5 | −8 | 20, 30, 50, 80, 120, 200, 300, 500, 800, 1200, 2000 | 0, 0.3, 0.5 | 975 | 100 | And XXIX |
| | −7 | 20, 30, 50, 80, 120, 200, 300, 500, 800, 1200 | | | 100 | Eri II, And XI |
| | −6 | 20, 30, 50, 80, 120, 200, 300, 500 | | | 100 | Hercules |
| | −5 | 20, 30, 50, 80, 120, 200 | | | 92 | Leo IV, Hydra II |
| | −4 | 20, 30, 50, 80, 120, 200 | | | 0 | Gru II, Pisces II |
| 3.5 | −11 | 3000, 5000 | 0, 0.3, 0.5 | 1180 | 100[a] | DDO113, Cetus |
| | −10 | 50, 80, 120, 200, 300, 500, 800, 1200, 2000, 3000 | | | 100 | Antlia B, And III |
| | −9 | 50, 80, 120, 200, 300, 500, 800, 1200, 2000 | | | 100 | Draco, Carina |
| | −8 | 50, 80, 120, 200, 300, 500, 800, 1200 | | | 95 | And XXIX |
| | −7 | 50, 80, 120, 200, 300 | | | 45 | Eri II, And XI |
| | −6 | 50, 80, 120, 200, 300 | | | 0 | Hercules |
| 5 | −11 | 2000, 3000 | 0, 0.3, 0.5 | 660 | 100[a] | DDO113, Cetus |
| | −10 | 80, 120, 200, 300, 500, 800, 1200, 2000, 3000 | | | 100 | Antlia B, And III |
| | −9 | 80, 120, 200, 300, 500, 800, 1200, 2000 | | | 97 | Draco, Carina |
| | −8 | 80, 120, 200, 300, 500, 800, 1200 | | | 50 | And XXIX |
| | −7 | 80, 120, 200, 300, 500, 800 | | | 0 | Eri II, And XI |

**Notes.** Column 1: fiducial distance at which simulated galaxies are injected. Column 2: absolute $V$-band magnitude of simulated galaxies. Column 3: elliptical half-light radii values that we use in our simulations. Column 4: ellipticity values used for each $M_V$ and $r_h$ value. Column 5: total number of simulated galaxies for each fiducial distance. Column 6: detection completeness for our simulated galaxies (injected into the NGC 253, low Galactic latitude data) in the range of 26 mag arcsec$^{-2}$ $\lesssim \mu_{V,0} \lesssim$ 29 mag arcsec$^{-2}$. Column 7: Local Group analogs that detectability ratio (%) approximately refers to.
[a] For $M_V = -11$, we only simulate galaxies with $\mu_{V,0} > 29$ mag arcsec$^{-2}$. Given that our simulated galaxies with $\mu_{V,0} = 30$ mag arcsec$^{-2}$ have an 80% recovery rate, we extrapolate the detectability here for the range of 26 mag arcsec$^{-2}$ $\lesssim \mu_{V,0} \lesssim$ 29 mag arcsec$^{-2}$.

compare our recovered structural parameters back to the true inputs and confirm that they are consistent within the uncertainties. Then, we derive the absolute magnitudes of our simulated galaxies following the same procedure as in Mutlu-Pakdil et al. (2018). In short, we build a well-populated CMD, including our completeness and photometric uncertainties, with the same isochrones used for our mock observations and their associated luminosity functions. We then randomly select the same number of stars from this artificial CMD as was found from our exponential profile fits. We sum the flux of these stars and extrapolate the flux of unaccounted stars using the adopted luminosity function. We calculate 100 realizations in this way and take the mean as our absolute magnitudes and the standard deviation as our uncertainties. We verify that our recovered luminosities and the true inputs agree well within the recovered uncertainties. As our focus in this paper is solely on detection, we will present the details of our investigation in a future paper. This will allow us to improve our current tools and properly interpret resolved stellar population studies in the Local Volume in the next-generation surveys.

### 3.2. Dwarf Recovery Using a Matched-filter Technique

Detecting resolved dwarf galaxies outside the Local Group is difficult because of their faint TRGB, low surface brightnesses, and small sizes. However, in deep, high-resolution data such as presented here and expected in future programs, most dwarf candidates can be identified by eye (if not near the detection limit) due to their compact size and underlying diffuse light contribution with clearly resolved stars overlaid. This can be seen in Figure 3 and those that follow it in this work. However, future surveys will cover thousands of square degrees, making visual inspection impossible. This motivated us to test the bounds of dwarf detectability in a quantifiable way using a matched-filter technique (Rockosi et al. 2002; Walsh et al. 2009), which maximizes the signal-to-noise ratio in possible dwarf stars over the background.

First, we build a well-populated signal CMD (of ≈75,000 stars), including our completeness and photometric uncertainties based on artificial star tests, by adopting the same isochrones used for our mock observations and their associated luminosity functions. For a fiducial distance of 1.5 Mpc, similar to our mock observations, we include HB stars in our signal CMD. For background CMDs, we use stars from the original image (before we inject artificial galaxies). An alternative background selection would be from a field well outside the body of each injected dwarf. However, this would make the background selection harder, especially for our experiments on very large, diffuse systems. We check the effects of different background selections and confirm that using the preinjection stars does not artificially enhance the detectability estimates relative to using a background annulus. We note that the matched-filter technique requires a well-defined background star CMD, and fortunately for future wide-field surveys, it should be straightforward to define stable background CMDs with large sky coverage.

We bin these CMDs into $0.1 \times 0.1$ color–magnitude bins. We then spatially bin our stars into 20″ pixels and smooth our final values using a Gaussian of the width of the pixel size. We experiment with different pixel sizes and smoothing scales and find that density maps with 20″ pixels are sensitive to dwarf galaxies with a wide range of properties. The background level (*sky_mean*) and variance (*sky_sigma*) of these smoothed maps are determined using the MMM routine in IDL. The normalized signal can be defined as $S = (smooth\_map - sky\_mean)/sky\_sigma$ and gives the number of standard deviations ($\sigma$) above the local mean. We adopt $S$ as a measure of detection signal. While creating matched-filter maps, we only include the stars with $r \leqslant 26.35$ mag (our 90% completeness limit in $r$).

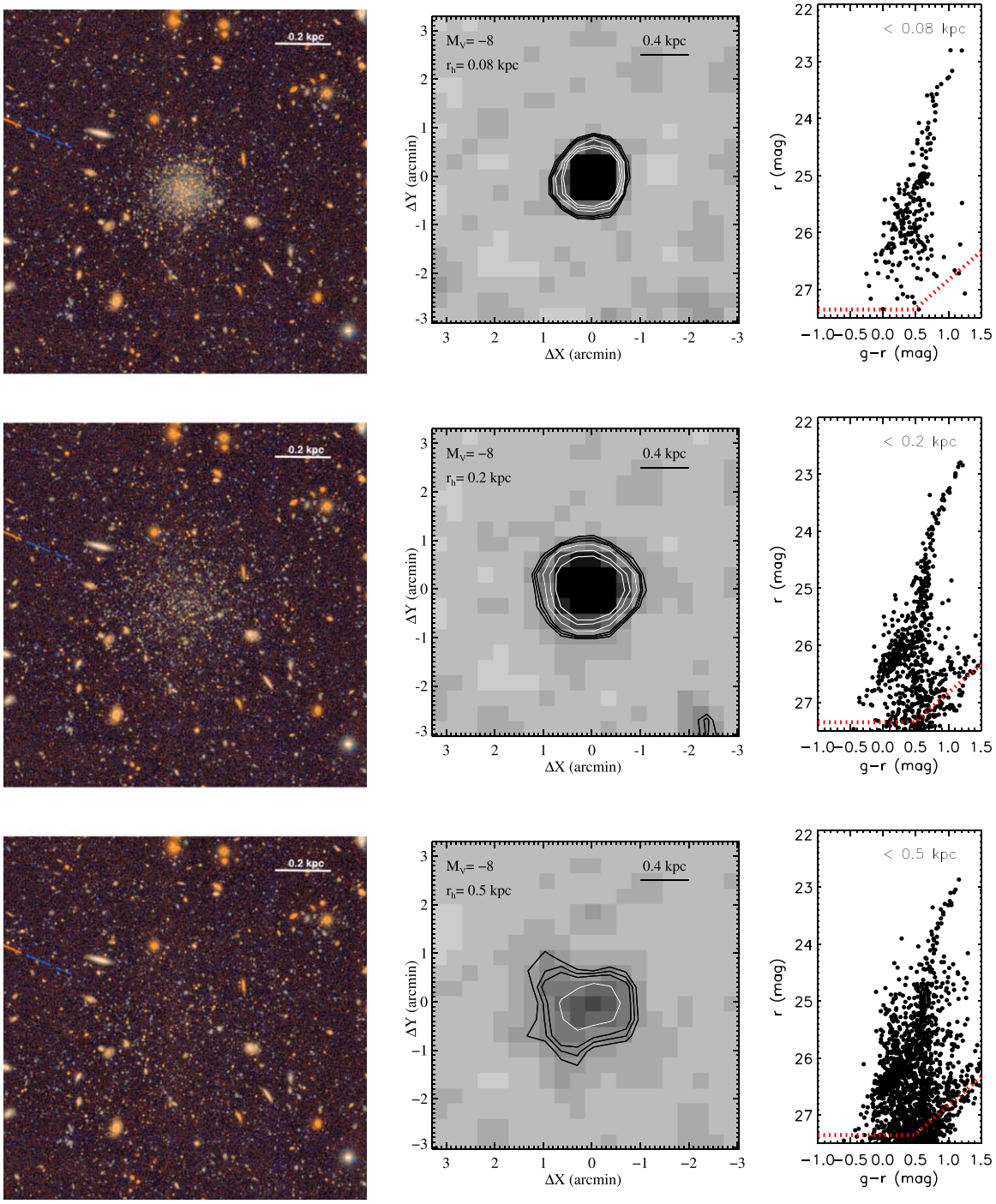


**Figure 4.** Example simulated resolved dwarfs with $M_V = -8$ at 1.5 Mpc, with increasing physical sizes from top ($\mu_{V,0} = 25$ mag arcsec$^{-2}$) to bottom ($\mu_{V,0} = 29$ mag arcsec$^{-2}$). The left panel displays false-color images. The middle panel is the smoothed matched-filter stellar density map, where we have spatially binned the input data and smoothed with a Gaussian of the width of the pixel size (20″). The contour levels show the 5$\sigma$, 6$\sigma$, 7$\sigma$, 10$\sigma$, 15$\sigma$, and 20$\sigma$ levels above the modal value. Right: CMDs, including stars within one half-light radius. The red line represents the 50% completeness limit, i.e., $r = 27.35$ mag.

Using a fainter magnitude limit increases the galaxy contamination in general and lowers the detection signal.

It is critical to gauge the significance of any given overdensity and define a detection threshold to eliminate false detections. To address this, we use our preinjection star catalog but randomize the star positions across the field of view according to a uniform distribution. We then create matched-filter maps of these random realizations, identically to that done above. We characterize the frequency and magnitude of purely random fluctuations in stellar density by measuring the maximum value of $S$ for 100 random realizations. We find that 3$\sigma$ overdensities are relatively common, with occasional 4$\sigma$ peaks. Therefore, we consider any stellar overdensity with $S \geqslant 5\sigma$ as a detection if its peak overlaps with the center of the simulated galaxy to within 0.′5. However, we allow a larger offset for low-density systems (i.e., offset $\leqslant 0.5 r_h$ if the $r_h$ is $>1'$) because the distribution of pixel values becomes non-Gaussian in such systems.

Figures 4–6 show a few examples of our simulated galaxies at each fiducial distance. The left panels display color images

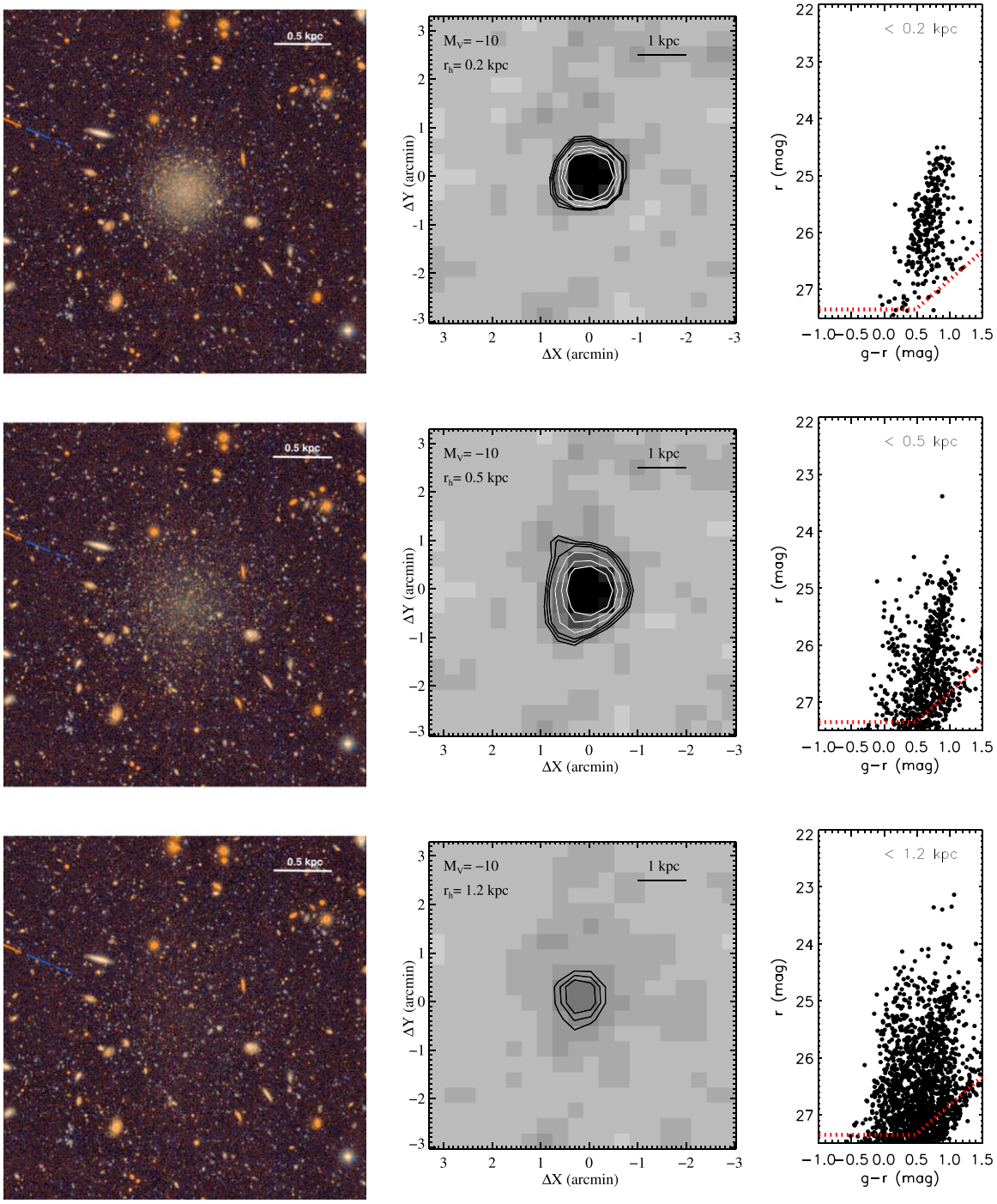


**Figure 5.** Example simulated resolved dwarfs with $M_V = -10$ at 3.5 Mpc, with increasing physical sizes from top to bottom. The left panel displays false-color images. The middle panel is the smoothed matched-filter stellar density map, where we have spatially binned the input data and smoothed with a Gaussian of the width of the pixel size (20″). The contour levels show the $5\sigma$, $6\sigma$, $7\sigma$, $10\sigma$, $15\sigma$, and $20\sigma$ levels above the modal value. Right: CMDs, including stars within one half-light radius. The red line represents the 50% completeness limit, i.e., $r = 27.35$ mag.

of simulated dwarfs, and they are arranged by increasing physical size from top to bottom. The middle panels are the smoothed matched-filter maps, where the contour levels show the $5\sigma$, $6\sigma$, $7\sigma$, $10\sigma$, $15\sigma$, and $20\sigma$ levels above the modal value. The right panels are the recovered CMDs, including stars within the half-light radius, $r_h$. The red line in the CMDs represents the 50% completeness limit, i.e., $r = 27.35$ mag. With similarly deep future observations, we will be able to reach stars at least ∼4.5 mag below the TRGB for a distance of up to 1.5 Mpc and ∼2 mag below the TRGB at 5 Mpc. This will enable us to detect new faint systems via stellar overdensities, as shown in the matched-filter maps.

In our stellar density maps, compact dwarf galaxies are more easily detected compared to extended, low surface brightness objects. As the physical size increases and a dwarf of a given luminosity is spread over a larger area, field contamination increases and the dwarf stellar population becomes less evident in the CMDs. As a result, the signal in the matched-filter maps decreases. On the other hand, stellar crowding becomes important for compact dwarfs, affects the photometric quality,

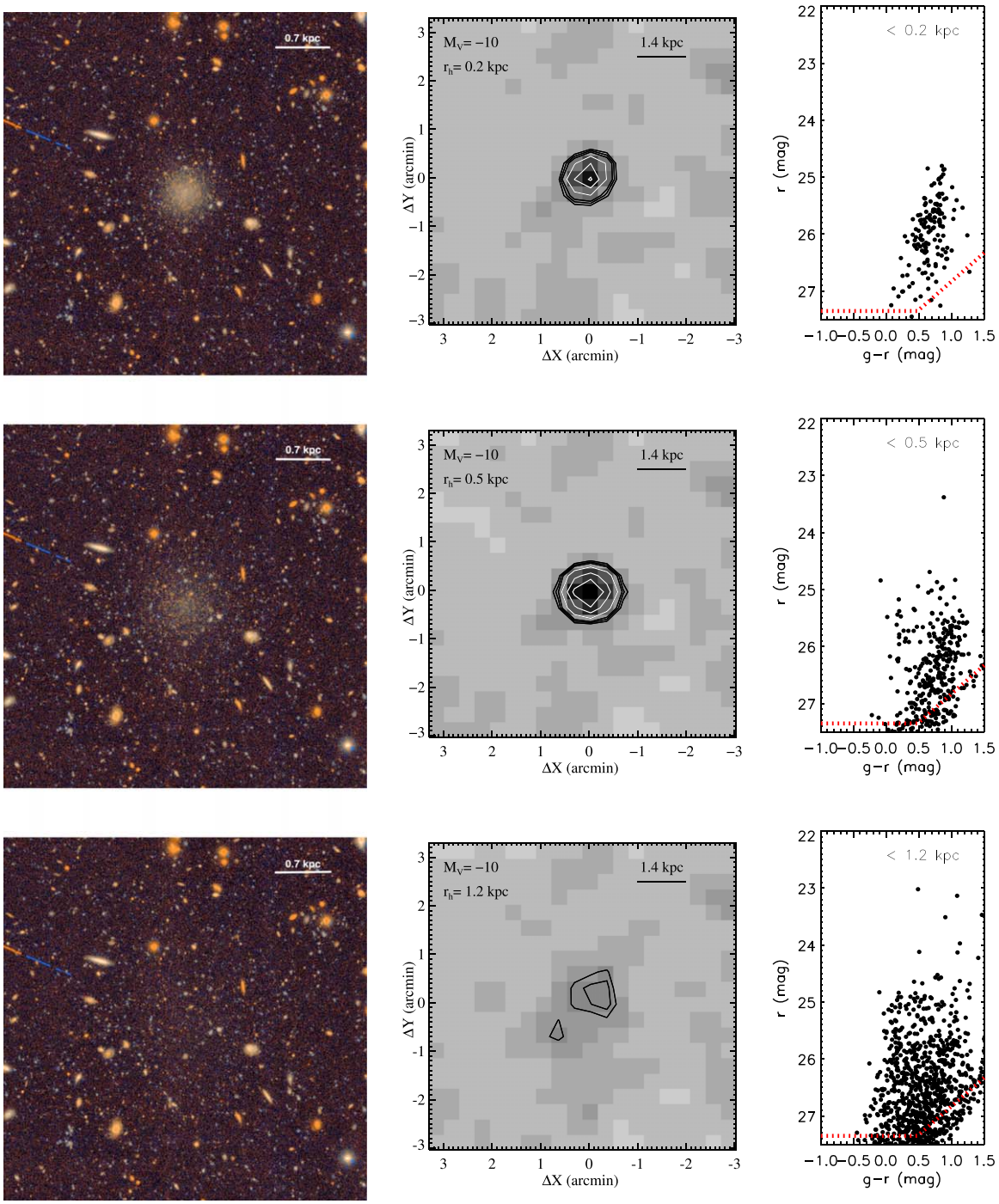


**Figure 6.** Example simulated resolved dwarfs with $M_V = -10$ at 5 Mpc, with increasing physical sizes from top to bottom. The left panel displays false-color images. The middle panel is the smoothed matched-filter stellar density map, where we have spatially binned the input data and smoothed with a Gaussian of the width of the pixel size (20″). The contour levels show the $5\sigma$, $6\sigma$, $7\sigma$, $10\sigma$, $15\sigma$, and $20\sigma$ levels above the modal value. Right: CMDs, including stars within one half-light radius. The red line represents the 50% completeness limit, i.e., $r = 27.35$ mag.

and decreases the number of recovered stars, especially at fainter magnitudes (see the top panels of Figures 4–6). As shown in the next section, the matched-filter technique is quite powerful in identifying both compact and extended systems, but it becomes unreliable when the system is so extended that the background overwhelms the dwarf stars or so compact that dwarf stars cannot be resolved due to crowding.

To gauge the varying effects of foreground stars and compact background galaxies on dwarf detection, our pipeline creates mock observations of the same galaxy at five different sky positions in the field. Overall recovery rates are very similar for each position. Varied local stellar densities affect the peak $S$ in the matched-filter maps at the $\sim$15% level, on average. This is valid for both low- and high-latitude systems (based on our tests on the NGC 253 and Cen A fields). Different stellar backgrounds become particularly important for extended systems and faint dwarfs, where the number density of dwarf stars in a region is low. A diffuse dwarf may be

detected in one position while the same galaxy may be below the detection threshold at another due to random noise from the foreground/background.

Finally, we check the effects of the shape of a dwarf galaxy on its detectability. Our pipeline creates mock observations with three different ellipticities, i.e., $\epsilon = 0$, 0.3, and 0.5 (see Figure 3). In general, rounder compact systems have higher detectability than their elongated analogs, and elongated larger systems are relatively easier to detect than their round counterparts. This is not surprising; as the ellipticity increases and the elliptical half-light radius is kept fixed, a dwarf of a given luminosity is spread over a smaller area. Higher ellipticity decreases the number of resolved stars for compact systems (due to higher blending), while it increases the number density of dwarf stars for larger systems. At $\mu_{V,0} \lesssim 24$ mag arcsec$^{-2}$, the detection signal of a dwarf with an ellipticity of 0.5 is ∼20% lower, on average, than that of its round analog. For brighter systems, this effect is much stronger, and the elongation can affect the detection signal at up to the ∼50% level. The opposite happens at $\mu_{V,0} \gtrsim 29$ mag arcsec$^{-2}$, where the detection signal of a dwarf with an ellipticity of 0.5 is ∼20% higher, on average, than that of its round analog. For fainter systems near the detection limit, the CMD shot noise becomes the dominant factor, and the effects of elongation are not systematic and barely noticeable.

## 4. Dwarf Discovery Space

Figures 7–9 report the results of our artificial resolved dwarf tests at distances of 1.5, 3.5, and 5 Mpc, respectively. The figures show the size–luminosity space probed by our tests,[15] where the colored blocks present the detection efficiency map of our simulated dwarfs. Each block represents ∼15 simulated dwarfs, on average. The blue hatched regions labeled as "100% Detected (Extrapolated)" denote the approximate regions where dwarfs should be easily detected and hence have not been explored in our simulations. Similarly, orange hatched regions labeled as "0% Detected (Extrapolated)" represent the approximate regions where we extrapolate that dwarfs will be undetectable. For convenience, in Table 2, we report the detection efficiency of each luminosity bin for 26 mag arcsec$^{-2} \lesssim \mu_{V,0} \lesssim 29$ mag arcsec$^{-2}$ at each fiducial distance. We also note Local Group analogs with similar properties in each row. Our experiments show that current and next-generation deep surveys will push the discovery frontier for new dwarf galaxies to fainter magnitudes, lower surface brightnesses, and larger distances.

### 4.1. Distance of 1.5 Mpc

Figure 7 focuses on the dwarf discovery space at a distance of 1.5 Mpc, in comparison to known Local Group dwarfs (red symbols). At this distance, we focus on five luminosity bins: $M_V = [-8, -7, -6, -5, -4]$. Based on an extrapolation of our simulations, we expect a 100% detection rate for systems brighter than $M_V = -8$ (blue hatched region) and a 0% detection rate for systems fainter than $M_V = -4$ (orange hatched region). It is worth mentioning that Antlia B ($D = 1.3$ Mpc, $M_V = -9.7$; Sand et al. 2015a; Hargis et al. 2020) was recently discovered, and it is quite plausible that there are further bright dwarfs waiting to be discovered. Local Group dwarfs populate a well-defined locus in the size–luminosity plane, with a spread of ∼4 mag arcsec$^{-2}$. While critically exploring this locus, we expand our investigation to higher and lower $\mu_{V,0}$ values. We note that we have not explored the gray region (labeled as "not explored" in the figure), which is mostly dominated by tidally stripped galaxy nuclei and luminous globular clusters. As these systems are very bright and compact, it is difficult to reliably identify them with our matched-filter technique due to high degrees of blending; hence, they are not the focus of this paper. However, a Gaia-based selection method introduced by Voggel et al. (2020) can serve as a powerful and complementary tool for finding and studying these bright compact objects out to distances of ∼25 Mpc.

We find that the overall completeness for $M_V \lesssim -5$ and 24 mag arcsec$^{-2} \lesssim \mu_{V,0} \lesssim 30$ mag arcsec$^{-2}$ is very high, with 90% of all injected dwarfs recovered. In particular, dwarfs with $\mu_{V,0} \lesssim 27$ mag arcsec$^{-2}$ will be easily detected with a high detection signal of $\sim 70\sigma$. While the detection rate for large and diffuse dwarfs like Crater 2 ($M_V = -8.2$, $r_h = 1066$ pc) is very high (87%), their detection significance is $\sim 10\sigma$. At $M_V \approx -8$, the detection signal stays above the threshold of $5\sigma$ down to $\mu_{V,0} \sim 32$ mag arcsec$^{-2}$.

More importantly, it will be possible to uncover ultrafaint satellite dwarfs like Hercules, Leo IV, and Hydra II (with a detection significance of $\sim 8\sigma$) at the edge of the Local Group. The secure census of ultrafaint satellite dwarfs will be possible down to $\mu_{V,0} \sim 30$ mag arcsec$^{-2}$ for $M_V = [-7, -6]$ and $\mu_{V,0} \sim 29$ mag arcsec$^{-2}$ for $M_V = -5$. This means we will be able derive the complete satellite luminosity functions (SLFs) of several nearby galaxies, including NGC 3109 (see Table 1), down to $M_V \approx -5$, providing important constraints on the physics of dark matter and galaxy formation on the smallest scales.

At $M_V = -4$, our simulated dwarfs are all below the detection threshold ($>5\sigma$), and none of them are recovered (0% detectability). We expect fainter systems to similarly stay hidden. Likewise, based on the trend of the detection signal as a function of luminosity and size, approximately 0% and 100% detection regimes are defined and shown in Figure 7 as orange and blue hatched regions, respectively.

### 4.2. Distance of 3.5 Mpc

Figure 8 shows our results for a distance of 3.5 Mpc. In addition to known Local Group dwarfs, we also include the known satellites of Cen A and NGC 253, both of which are located at ∼3.5 Mpc (orange symbols). Here we mostly focus on five luminosity bins: $M_V = [-10, -9, -8, -7, -6]$. At this distance, all observed, known dwarfs have surface brightnesses $\mu_{V,0} \lesssim 28$ mag arcsec$^{-2}$, and our experiments demonstrate that similar objects will be easily detectable in the matched-filter maps (100% detectability); while the detection signal is $\sim 15\sigma$ for the faintest ones ($M_V \approx -8$), it is $\gtrsim 50\sigma$ for brighter ones ($M_V \lesssim -9$).

Most notably, a secure census of faint dwarf galaxies down to $M_V \approx -7$ will be possible up to 3.5 Mpc. In particular, at $M_V = -8$ and 25 mag arcsec$^{-2} \lesssim \mu_{V,0} \lesssim 29$ mag arcsec$^{-2}$, the recovery fraction is very high, with 90% of all injected dwarfs recovered. However, large and diffuse systems like Crater 2 ($M_V = -8.2$, $r_h = 1066$ pc) and And XIX ($M_V = -9.2$, $r_h = 1683$ pc) stay below the detection limit ($<5\sigma$, 0% detectability). At $M_V = -7$ and 26 mag arcsec$^{-2} \lesssim \mu_{V,0} \lesssim 28$ mag arcsec$^{-2}$, detectability is still high ($\gtrsim 50\%$), but the recovery rate decreases quickly at higher and lower $\mu_{V,0}$ values. Given the small number of dwarf stars,

[15] We use the input values of size and luminosity in these figures.

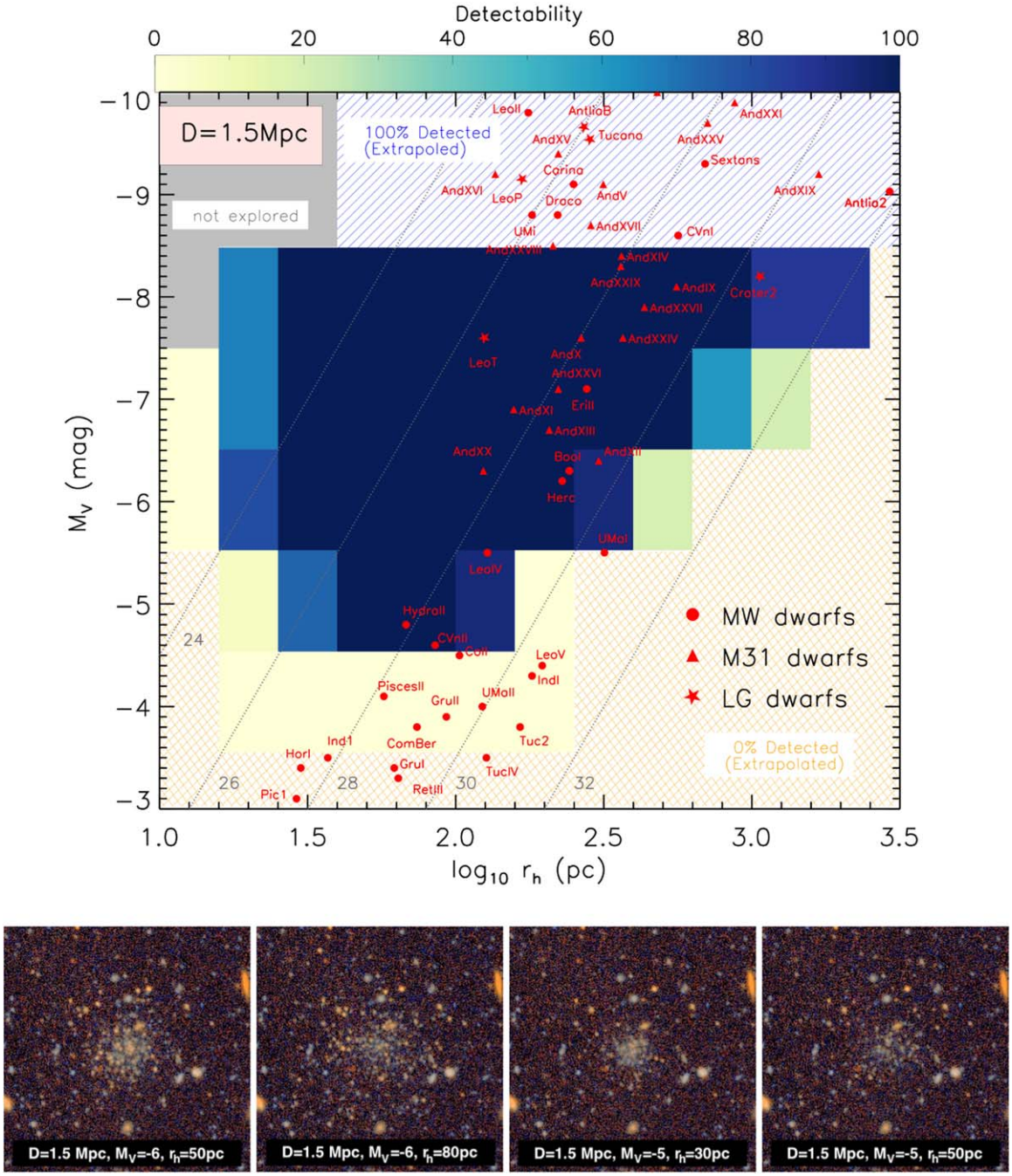





**Figure 7.** Top: results of our artificial resolved dwarf tests at a distance of 1.5 Mpc. It shows the size–luminosity phase space probed by our tests, along with known satellites of the Local Group (circles, MW dwarfs; triangles, M31 dwarfs; stars, other Local Group dwarfs). Lines of constant *V*-band surface brightness are shown at 24, 26, 28, 30, and 32 mag arcsec$^{-2}$. Colored regions show the recovery efficiency for our simulated dwarfs in size–luminosity space. The blue hatched area at bright magnitudes denotes the approximate region where dwarfs should be easily detected (with ∼100% efficiency), while the orange hatched region corresponds to regions with little chance of dwarf detection (with a presumed 0% recovery); we have not explicitly explored these regions with our simulations. Bottom: RGB false-color images of simulated ultrafaint dwarf galaxies. For each image cutout, the size is $1' \times 1'$. Our experiments show that dwarfs as faint as these will be detectable at ∼1.5 Mpc.

stellar crowding prevents stars from being resolved in compact systems, while the background overwhelms the number density of dwarf stars in large, diffuse systems.

It will be crucial to uncover bright ultrafaint dwarfs ($-8 \lesssim M_V \lesssim -7$) at this distance, as they will serve as a comparison for known Local Group dwarfs and allow for measurements as a function of galaxy environment, halo mass, and morphology and to determine the typical halo-to-halo scatter. Fainter ultrafaint systems ($M_V \gtrsim -6$) have only a handful of resolved stars at this distance and stay hidden in the stellar density maps (0% detectability).

It is worth mentioning that the results here come from the NGC 253 data, where the MW contamination is very low. In Section 4.4, we explore the effects of MW contamination and foreground extinction on dwarf detection by rerunning our experiments at a distance of 3.5 Mpc on the Cen A data.

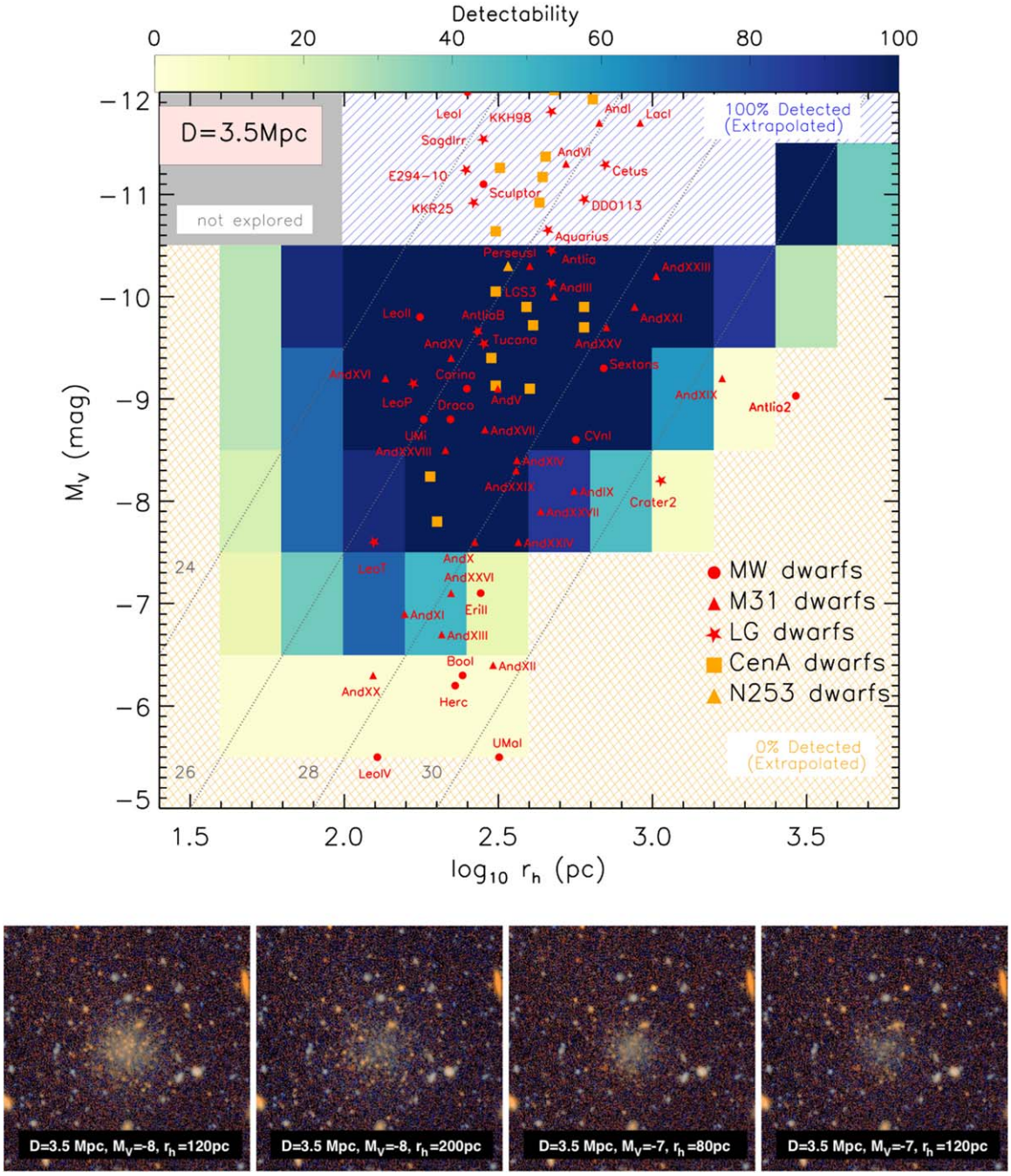


**Figure 8.** Top: results of our artificial resolved dwarf tests at a distance of 3.5 Mpc. It shows the size–luminosity space probed by our tests, along with known Local Group dwarfs (red symbols), Cen A dwarfs (orange squares), and NGC 253 dwarfs (orange triangles). Lines of constant *V*-band surface brightness are shown at 24, 26, 28, and 30 mag arcsec$^{-2}$. The colored region shows a recovery completeness map for our simulated dwarfs in size–luminosity space. The blue hatched area at bright magnitudes denotes the approximate region where dwarfs should be easily detected (with ∼100% efficiency), while the orange hatched region corresponds to regions with little chance of dwarf detection (with a presumed 0% recovery); we have not explicitly explored these regions with our simulations. Bottom: RGB false-color images of example simulated faint dwarf galaxies. For each image cutout, the size is $1' \times 1'$. Our experiments show that dwarfs as faint as these will be detectable out to 3.5 Mpc.

### *4.3. Distance of 5 Mpc*

Figure 9 shows our results for a distance of 5 Mpc. In addition to Local Group dwarfs and known satellites of Cen A and NGC 253, we also include the M94 faint satellites, which are located at ∼4.5 Mpc (orange stars). Here we mostly focus on four luminosity bins: $M_V = [-10, -9, -8, -7]$. At this distance, simulated dwarfs with properties similar to the known, observed dwarf data set have a very high recovery rate (with 97% of all injected dwarfs recovered). At $M_V = -10$, most known objects have $\mu_{V,0}$ values between 26 and 28 mag arcsec$^{-2}$, and their analogs at 5 Mpc are very prominent in the matched-filter maps with $\sim 25\sigma$. Similarly, Leo II–like compact objects ($M_V = -9.8$, $r_h = 176$ pc) will be easily detected as $\sim 20\sigma$ stellar overdensities, while larger systems like And XXIII ($M_V = -10.2$, $r_h = 1029$ pc) and And XXI ($M_V = -9.9$, $r_h = 875$ pc) will be identified at the $\sim 15\sigma$ level. There are several known objects with $M_V \sim -9$ and $\mu_{V,0} \sim 26$ mag arcsec$^{-2}$—e.g., Draco, Leo P, Ursa Minor, and

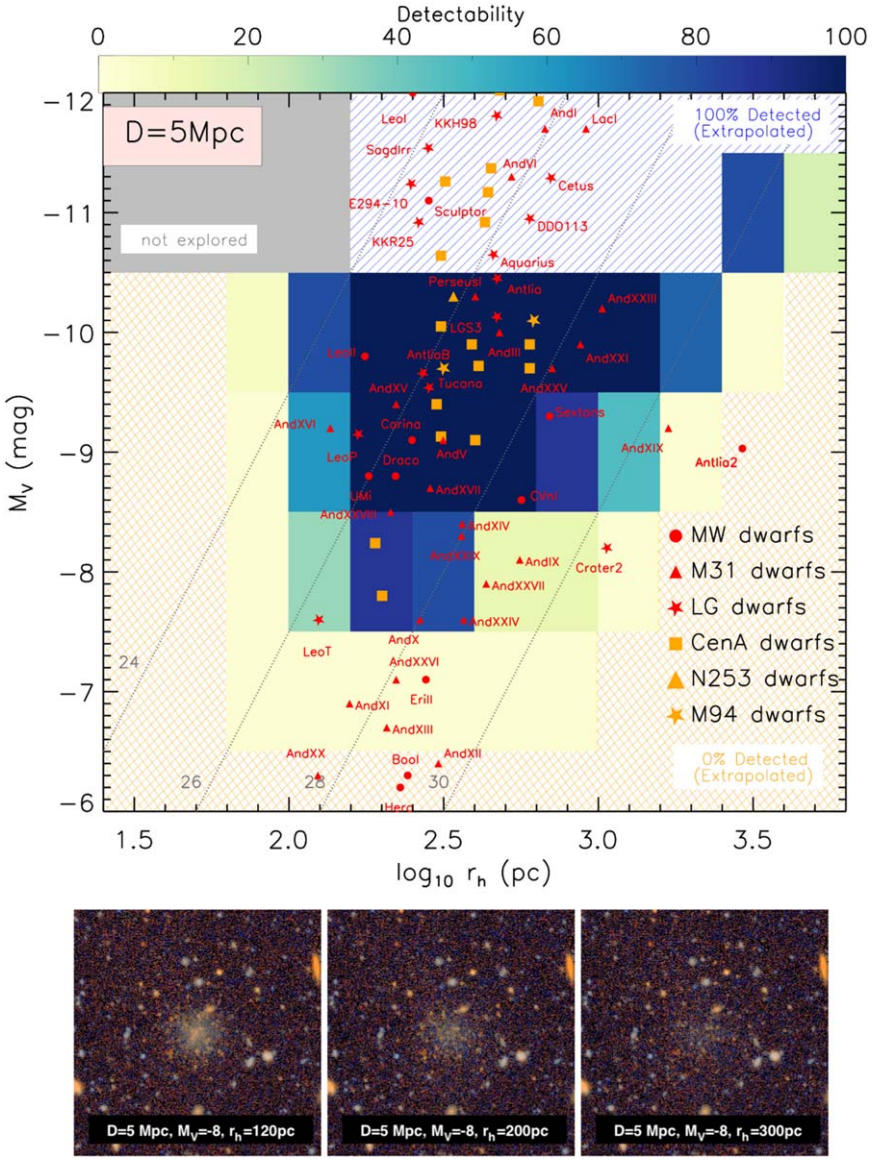


**Figure 9.** Top: results of our artificial resolved dwarf tests at a distance of 5 Mpc. It shows the size–luminosity space probed by our tests, along with known Local Group dwarfs (red symbols), Cen A dwarfs (orange squares), NGC 253 dwarfs (orange triangles), and M94 dwarfs (orange stars). Lines of constant *V*-band surface brightness are shown at 24, 26, 28, and 30 mag arcsec$^{-2}$. The colored region shows the recovery completeness map for our simulated dwarfs in size–luminosity space. The blue hatched area at bright magnitudes denotes the approximate region where dwarfs should be easily detected (with ∼100% efficiency), while the orange hatched region corresponds to regions with little chance of dwarf detection (with a presumed 0% recovery); we have not explicitly explored these regions with our simulations. Bottom: RGB false-color images of example simulated faint dwarf galaxies. For each image cutout, the size is $1' \times 1'$. Our experiments show that dwarfs as faint as these will be detectable out to 5 Mpc.

Carina—and the detection rate of their analogs is 100% with a significance of $\sim 15\sigma$.

Overall, we find that a secure census of faint dwarf galaxies down to $M_V \approx -8$ will be possible up to 5 Mpc. The completeness is very high for $M_V \lesssim -9$ down to $\mu_{V,0} \sim 30$ mag arcsec$^{-2}$, and it stays high for $M_V \approx -8$ in the range 26 mag arcsec$^{-2}$ $\lesssim \mu_{V,0} \lesssim$ 28 mag arcsec$^{-2}$ (with a detection signal of $\sim 7\sigma$). In addition, it will be possible to detect some of the compact systems with $\mu_{V,0} \sim 26$ mag arcsec$^{-2}$ (33% detectability) and a few low surface brightness cases like And IX ($M_V = -8.1$, $r_h = 557$ pc, 13% detectability) at this distance. In our experiments, ultrafaint dwarf galaxies ($M_V \gtrsim -7$) stay below the detection limit (0% detectability).

Interestingly, there are currently no known dwarfs with $\mu_{V,0} \gtrsim 27$ mag arcsec$^{-2}$ at the absolute magnitude range of $-12 \lesssim M_V \lesssim -10.5$. We perform an additional test at $M_V = -11$ with $\mu_{V,0} = [30, 31]$ mag arcsec$^{-2}$. The completeness of very large, diffuse systems down to $\mu_{V,0} = 30$ mag arcsec$^{-2}$ is very high, with a detection signal of $\sim 8\sigma$ (e.g., 80% detectability), and it is possible to detect some of the sytems with $\mu_{V,0} = 31$ mag arcsec$^{-2}$ (20% detectability). Based on our tests, we expect LSST- (or HSC)-like observations to be sensitive to dwarfs at this unexplored regime out to 5 Mpc.

### 4.4. Effects of MW Contamination and Extinction

The results presented here so far come from the chosen NGC 253 pointing, which is located at a high Galactic latitude ($b = -88°$) such that the foreground extinction is very low ($E(B-V) = 0.02$). However, there are many galaxies within 5 Mpc that are located at a low Galactic latitude with higher

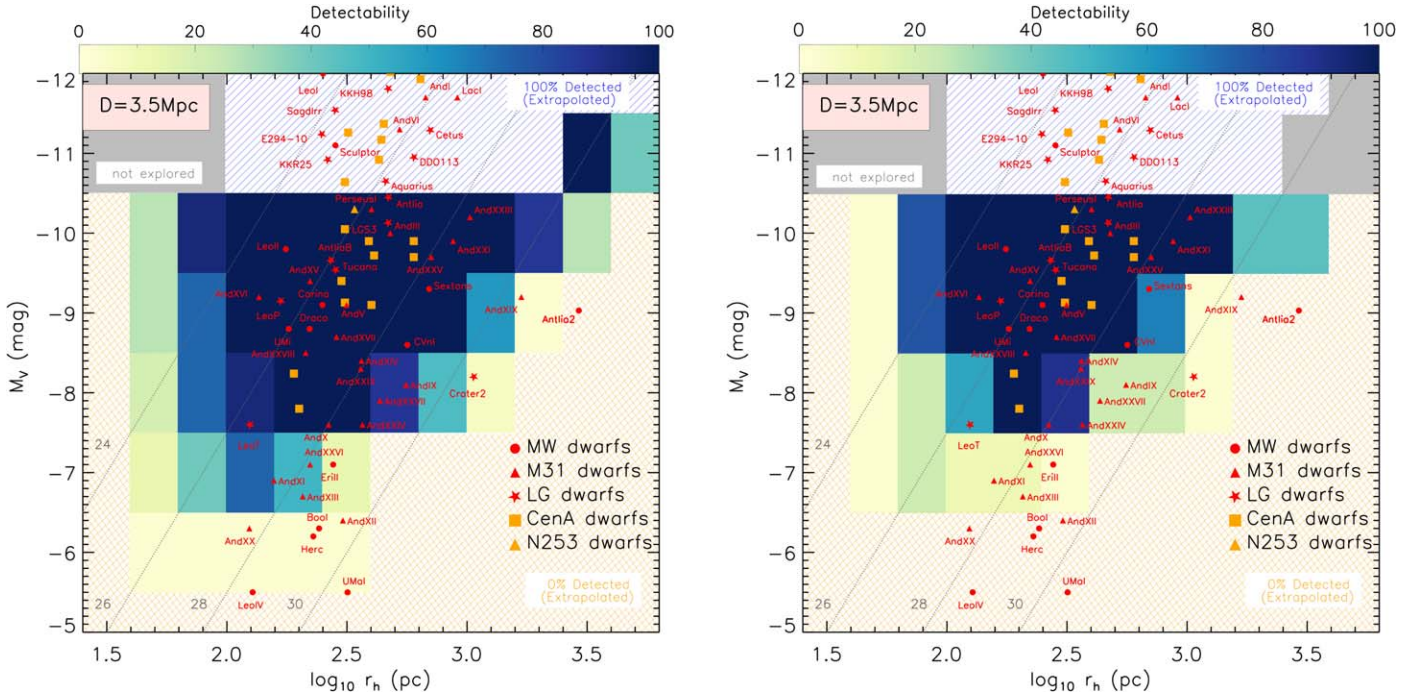


(a) High Latitude Case: NGC 253 field (b) Low Latitude Case: Cen A field

**Figure 10.** We use the best imaging field of Cen A ($b = 19°$, $E(B-V) = 0.12$) to assess the effects of MW disk contamination and extinction in detecting dwarf galaxies. (a) Same as Figure 8 and shown here just for comparison reasons. (b) Our Cen A simulation results for a distance of 3.5 Mpc, demonstrating that both extinction and foreground MW star counts may strongly affect dwarf detectibility, especially for low surface brightness systems ($\mu_{V,0} \gtrsim 29$ mag arcsec$^{-2}$) and objects fainter than $M_V \approx -8$.

extinction (see Table 1). Therefore, we repeat a subset of dwarf simulations by using the best imaging field from PISCeS of Cen A ($b = 19°$, $E(B-V) = 0.12$) to assess the effects of MW disk contamination and extinction in detecting dwarf galaxies. Because the extinction is highly correlated to the Galactic latitude, our experiment here probes their combined effects.

Figure 10 presents our Cen A simulation results for a distance of 3.5 Mpc. For comparison, we redisplay our results of the NGC 253 field at the same distance (Figure 8) in panel (a). For the size–luminosity space where all distant dwarfs are located (orange symbols), detection completeness stays the same, with a very high recovery rate (100%). However, compared to our NGC 253 experiments, the overall detection signal is ∼20% lower, on average, in the Cen A data. The effects become especially important for systems with a detection significance of $\lesssim 7\sigma$ in our NGC 253 experiments, e.g., low surface brightness systems ($\mu_{V,0} \gtrsim 29$ mag arcsec$^{-2}$) and objects fainter than $M_V \gtrsim -8$. For example, the detectability of compact objects (e.g., $M_V \sim -8$, $r_h \sim 120$ pc) decreases to 55% from 95%, while systems like And XI ($M_V = -6.9$, $r_h = 157$ pc) decrease to 10% from 45%.

## 5. Discussion

To fully test the ΛCDM paradigm and constrain the physics governing galaxy formation and evolution at the smallest scales, we need comprehensive investigations into the abundance and properties of dwarf galaxies around primary galaxies with different masses, morphologies, and environments. In Table 1, we compile a list of nearby galaxies within ≈5 Mpc, which we can study in detail with resolved stellar populations with current state-of-the-art telescope facilities. Within the MW luminosity group, beyond the Local Group, dedicated deep wide-field surveys exist for Cen A (Crnojević et al. 2016, 2019 with Magellan/Megacam), NGC 253 (Sand et al. 2014; Toloba et al. 2016; B. Mutlu-Pakdil et al. 2021, in preparation, with Magellan/Megacam), M94 (Smercina et al. 2018 with Subaru/HSC), and M81 (including the M82 region; Chiboucas et al. 2009, 2013 with CFHT/MegaCam; Okamoto et al. 2019 with Subaru/HSC). The average seeing FWHM of these surveys is ∼0.″8. With systematic resolved stellar searches in these deep surveys, the faintest dwarfs discovered so far are CenA-MM17-Dw10 ($M_V = -7.8$, $r_h = 250$ pc; Crnojević et al. 2019) in the Cen A group and d0944+69 ($M_V = -8.1$, $r_h = 130$ pc; Chiboucas et al. 2013) in the M81 group, and they are consistent with our experiments at a distance of 3.5 Mpc (see Figures 8 and 10).

In Figure 11 (top panel), we show a comparison of the observed SLFs of these nearby galaxies to the theoretical expectations from Dooley et al. (2017b). For the observed luminosity functions, we adopt the Crnojević et al. (2019) compilation, which includes objects within 300 kpc of each host. These SLFs should be considered as a lower limit due to incomplete spatial coverage; while the MW SLF suffers due to our limited ability to detect satellites near the Galactic plane, other systems have not yet been mapped out to their virial radii (see Table 1; most deep wide-field surveys are limited to a radius of approximately 150 kpc). Note that we make no attempt to correct any luminosity function for incompleteness. The region where the Cen A and M81 SLFs become incomplete (in luminosity) are shown with open symbols and dashed lines (as reported by Crnojević et al. 2019 and Chiboucas et al. 2013). For theoretical predictions, we use the satellite stellar mass functions of Dooley et al. (2017b; see their Figure 5), which were derived by applying the abundance-

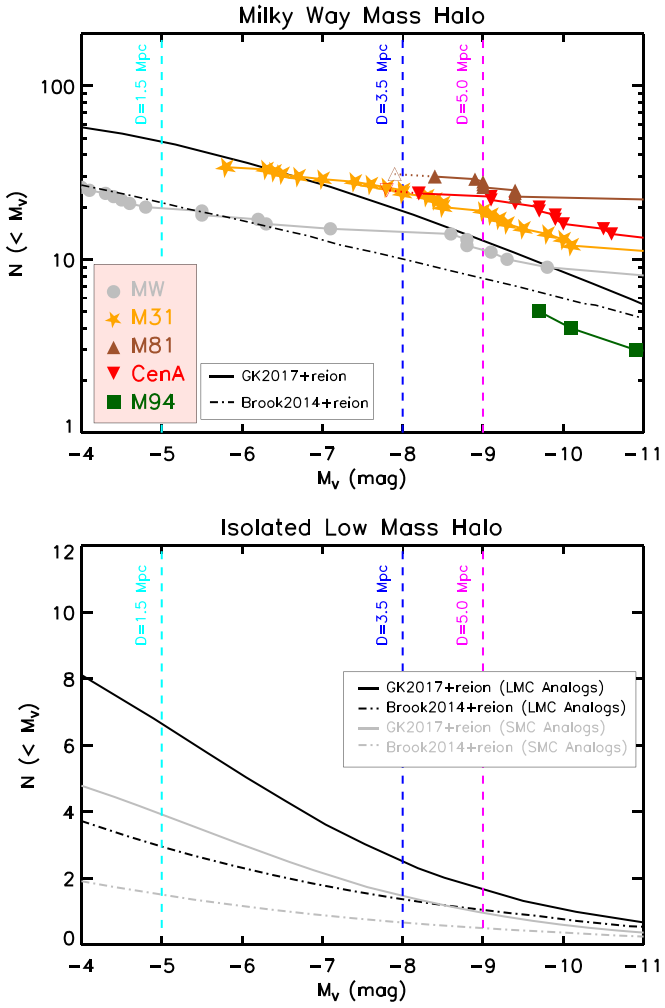


**Figure 11.** Top: mean number of satellites around an MW-mass halo as a function of the minimum satellite absolute magnitude. Solid and dotted–dashed lines are the predictions from Dooley et al. (2017b), based on Garrison-Kimmel et al. (2017, GK2017+reion) and Brook et al. (2014, Brook2014+reion), respectively. The data for the observed luminosity functions come from the Crnojević et al. compilation. The regions where the Cen A and M81 luminosity functions become incomplete are shown with hollow symbols and dashed lines. We mark our $\gtrsim$90% completeness limit for each distance fiducial (cyan: 1.5 Mpc, blue: 3.5 Mpc, magenta: 5 Mpc). Bottom: predicted mean number of satellites around an isolated low-mass host as a function of the minimum satellite absolute magnitude from Dooley et al. (2017a; black: LMC-mass host, gray: SMC-mass host).

matching models of Garrison-Kimmel et al. (2017) and Brook et al. (2014) and a reionization model to the dark matter–only Caterpillar simulation suite. We derive the luminosity functions from the stellar mass functions by assuming a stellar mass-to-light ratio of 1 and calculating $V$-band absolute magnitudes from luminosities. As stated by Dooley et al. (2017b), numbers predicted by the Brook et al. models represent the low end of the possibilities for dwarf satellite galaxies, and values from the Garrison-Kimmel et al. model are closer to median expectations. We observe a clear, large scatter in the observed luminosity functions at fixed magnitude, and we need a larger sample of dwarf satellites to determine the typical halo-to-halo scatter and ultimately constrain the models. In Figure 11, we also mark our $\gtrsim$90% detection completeness limit[16] for each fiducial distance. With the near-future surveys, it will be possible to go significantly further down the luminosity functions of nearby galaxies.

As is obvious from their high $A_V$ values, several galaxies located in the zone of Galactic obscuration (e.g., IC 342, Circinus) are not suitable for such resolved studies. More promising targets are M83, M64, and NGC 4945, and future dedicated surveys of their halos will extend our general knowledge of substructure not only to new systems but also to new environments. The tidal index parameter, $\Theta_5$, can be used as a measure of environment (Karachentsev et al. 2013), and $\Theta_5 < 0$ indicates an isolated galaxy. Interestingly, recent studies indicate a tentative relationship between satellite richness and environment, suggesting that isolated MW-like galaxies have fewer satellites and a higher overall star formation fraction than their counterparts in dense environments (Bennet et al. 2019). This is also in general agreement with the SAGA spectroscopic survey results (Geha et al. 2017; Mao et al. 2021), which focused on isolated MW-like galaxies at $D = 20$–$40$ Mpc and found a high fraction of star-forming dwarfs in their sample (note that they are limited to $M_V \lesssim -12$). These satellite population trends with environment may indicate that external processes such as tidal/ram pressure stripping are a physical driver of dwarf galaxy evolution. However, these results hinge on two nearby and relatively isolated galaxies: M94 ($D = 4.41$ Mpc, $\Theta_5 = 0.1$) and M101 ($D = 6.95$ Mpc, $\Theta_5 = 1.3$).[17] As shown in Section 4, a complete census of dwarf galaxies around M83, M64, and NGC 4945 is possible down to $M_V \approx -7$ or $-8$. In particular, as M64 ($D = 4.41$ Mpc, $\Theta_5 = -0.7$) and M83 ($D = 4.90$ Mpc, $\Theta_5 = 0.8$) are in low-density environments, they provide us with a unique opportunity to extend the range of environments probed by the existing surveys of nearby galaxies and quickly establish whether or not recent satellite environmental trends are valid or if a new physical mechanism is necessary to explain the recently measured halo-to-halo scatter at the faint end of the SLF.

In addition to the MW luminosity group, it is essential to explore dwarf satellites around low-mass galaxies to better constrain the $M_\star$–$M_{\rm halo}$ relationship. Cosmologically motivated models predict two to five and one to three satellites with $M_V \lesssim -7.7$ around LMC- and SMC-sized galaxies, respectively (Dooley et al. 2017a). In Figure 11 (bottom panel), we highlight our $\gtrsim$90% detection completeness limit for each distance fiducial. With the current and near-future ground-based instrumentation, we can test these predictions by performing systematic resolved stellar searches around the LMC/SMC analogs listed in Table 1. If we only focus on systems with an $A_V$ value of $<$0.5, there are 19 LMC analogs and 36 SMC analogs within 5 Mpc that are suitable for such studies. There is already a significant ongoing effort to map out the halos of several low-mass galaxies and search for their satellite populations, e.g., the Pan-Andromeda Archaeological Survey around M33 (for which only $\sim$half of the virial radius was mapped with CFHT/MegaCam, and two possible satellites have been reported so far; Martin et al. 2009, 2013; Martinez-Delgado et al. 2021), the Magellanic Analog Dwarf Companions And Stellar Halos (MADCASH) Survey (which is an ongoing DECam+HSC deep imaging campaign around a dozen relatively isolated nearby low-mass galaxies, where three

[16] Here we derive the completeness limits in the range of 26 mag arcsec$^{-2}$ $\lesssim \mu_{V,0} \lesssim$ 29 mag arcsec$^{-2}$.

[17] Due to its distance, the dwarf satellite search around this system has been conducted in integrated light surveys.

satellites have been reported to date: one around NGC 2403, one around NGC 4214, and one around NGC 3109; Sand et al. 2015a; Carlin et al. 2016, 2021), and DELVE-DEEP (which aims to obtain deep DECam imaging around Sextans B, IC 5152, NGC 55, and NGC 300; Drlica-Wagner et al. 2021). While the current campaigns focus on field dwarf galaxies, near-future studies present a great opportunity to target all 55 low-mass galaxies within 5 Mpc and explore the environmental effects on substructure properties at this mass scale. Based on the predictions of Dooley et al. (2017b), near-future studies are expected to find ∼(24–63, 14–110, 19–129) new satellites with $M_V \lesssim (-5, -8, -9)$ out to ∼(1.5, 3.5, 5) Mpc when these LMC/SMC analogs are mapped out to their virial radii. These studies will also be able to detect fainter dwarfs down to $M_V \approx -7$ and $-8$, with ∼50% completeness, out to 3.5 and 5 Mpc, respectively (see Table 2). In particular, M33, M32, IC 1613, NGC 205, and NGC 3109 are excellent examples where we can establish secure satellite populations down to $M_V \approx -5$ (due to their proximity), providing strong quantitative constraints on the $M_\star$–$M_{\rm halo}$ relationship.

While we mostly focus on the discovery space of dwarf satellites around Local Volume galaxies ($\lesssim$5 Mpc), LSST and other deep imaging surveys will also enable discovery of isolated dwarf galaxies that to date have been impossible without wide-area coverage. In particular, LSST will expand the sky coverage and volume over which our matched-filter technique can be applied. Isolated dwarf galaxies provide a unique reference group to disentangle environmental galaxy formation processes, as they live in fields isolated from galaxy groups where the environmental effect on galaxy processes is expected to be minimal (e.g., Dickey et al. 2019).

In this work, we examine the distance range where we can probe with resolved stars from the ground in the next decade. For the distances where this is not possible, surface brightness fluctuations provide a complementary tool to identify dwarf galaxies out to ∼25 Mpc (Greco et al. 2021). New and upcoming ground-based imaging surveys will make it possible to explore larger volumes with greater sensitivity, providing a large, rigorous census of faint galaxies across a wide range of environments, which will be crucial for our understanding of dark matter and galaxy formation.

## 6. Conclusions

In this work, we investigate the prospects for identifying resolved, faint dwarf galaxies within 5 Mpc with current and near-future ground-based instrumentation (e.g., Rubin, HSC). We perform image-level simulations of resolved, faint dwarf galaxies at three fiducial distances—1.5, 3.5, and 5 Mpc—with varying luminosities, ellipticities, sizes, stellar backgrounds, and galactic latitudes, utilizing the deep and high-quality imaging from the PISCeS data set. Then, we rigorously quantify the detectability of faint dwarf galaxies using a matched-filter technique. Our primary results may be summarized as follows.

1. The matched-filter technique is quite powerful for identifying both compact and extended systems, but it becomes unreliable when systems are so extended that the background overwhelms the dwarf stars or so compact that the dwarf stars cannot be resolved due to image crowding.
2. We probe the effects of local stellar densities in dwarf detection by placing dwarfs in different spatial positions. Varied stellar backgrounds affect the peak $S$ in the matched-filter maps at about the 15% level, on average. This becomes particularly important for extended systems and faint dwarfs, where the number density of dwarf stars is low.
3. We assess the effects of the ellipticity in dwarf detection by creating mock observations with three different ellipticities, i.e., $\epsilon = 0$, 0.3, and 0.5 (see Figure 3). At fixed $r_h$ and $M_V$, we find that rounder compact systems have a higher detectability ratio than their elongated analogs, and that elongated larger systems are relatively easier to detect than their round counterparts.
4. At a fiducial distance of 1.5 Mpc, current and next-generation deep surveys will be able to resolve HB stars (see Figure 2), making it possible to uncover ultrafaint satellite dwarfs like Hercules, Leo IV, and Hydra II at the edge of the Local Group. A secure census of ultrafaint satellite dwarfs will be possible down to $\mu_{V,0} \sim 30$ mag arcsec$^{-2}$ for $M_V = [-7, -6]$ and $\mu_{V,0} \sim 29$ mag arcsec$^{-2}$ for $M_V = -5$ (see Figure 7).
5. At a distance of 3.5 Mpc, similar-depth surveys will be able to probe ∼2.5 mag below the TRGB, enabling a secure census of faint dwarf galaxies to $M_V \lesssim -7$ (see Figure 5).
6. At a distance of 5 Mpc, it will be possible to reach ∼2 mag below the TRGB, enabling a secure census of faint dwarf galaxies down to $M_V \approx -8$. The detection completeness is very high for $M_V \lesssim -9$ down to $\mu_{V,0} \sim 30$ mag arcsec$^{-2}$, and it stays high for $M_V \approx -8$ in the range 26 mag arcsec$^{-2} \lesssim \mu_{V,0} \lesssim 30$ mag arcsec$^{-2}$ (see Figure 6).
7. We perform our experiments primarily on a pointing close to NGC 253, which is located at a high Galactic latitude ($b = -88°$, $E(B-V) = 0.02$). To assess the effects of MW disk contamination and extinction in detecting dwarf galaxies, we repeat a subset of dwarf simulations by using the Cen A data ($b = 19°$, $E(B-V) = 0.12$). The overall detection signal is ∼20% lower, on average, in our Cen A experiments. The effects become especially important for systems with a detection significance of $7\sigma$ in our NGC 253 experiments, e.g., low surface brightness systems ($\mu_{V,0} \gtrsim 29$ mag arcsec$^{-2}$) and objects fainter than $M_V \approx -8$ (see Figure 10).
8. Within the MW luminosity group, beyond the Local Group, the next ideal targets are M83, M64, and NGC 4945, which can extend our knowledge of substructure to new environments and quickly establish whether recent tentative relationships between satellite richness and environment are valid (Bennet et al. 2019).
9. Near-future studies present a great opportunity to target all 55 suitable low-mass galaxies within 5 Mpc (see Table 1 with $A_V < 0.5$) and explore the environmental effects on substructure properties at this mass scale. In particular, M33, M32, IC 1613, NGC 205, and NGC 3109 are great examples where we can establish secure satellite populations down to $M_V \approx -5$.

It is worth remembering that our simulations represent a set of idealized experiments. Here we assume that dwarf galaxies are pure single-stellar populations, following a smooth exponential stellar profile. While these assumptions are

reasonable for Local Volume dwarfs, they do not fully capture the potentially complex structure of dwarf galaxies, as studies of Local Group dwarfs have revealed (e.g., Sand et al. 2012; Muñoz et al. 2018; Mutlu-Pakdil et al. 2018, among others). In addition, we assume that the underlying stellar population of the host halo is low or negligible. However, the completeness of the dwarf search is expected to be lower in the inner regions of the parent galaxy due to halo contamination. The effect would be strongest for the largest, low surface brightness dwarfs for a given luminosity. That said, simulations with realistic baryonic effects predict few subhalos within 20 kpc (e.g., Garrison-Kimmel et al. 2017). Future work should explore these effects and carefully characterize detection limits near the parent galaxy.

Notwithstanding the above caveats, our experiments show that near-future studies, which will probe substantially deeper than previous data sets, will push the discovery frontier for new dwarf galaxies to fainter magnitudes, lower surface brightnesses, and larger volumes. These discoveries will extend the faint end of the SLF of numerous nearby galaxies with a range of masses, morphologies, and environments, which will allow us to quantify the statistical fluctuations in satellite abundances around hosts and parse environmental effects as a function of host properties. Ultimately, the goal is to understand galaxy formation and test the ΛCDM model on small scales.

We thank the anonymous referee for constructive comments that helped to improve this paper. We are grateful to P. Bennet for useful discussions and tabulated data that were used in this paper.

B.M.P. is supported by an NSF Astronomy and Astrophysics Postdoctoral Fellowship under award AST-2001663. J.D.S. acknowledges support from NSF grant AST-1412792. J.S. acknowledges support from NSF grant AST-1812856 and the Packard Foundation. D.J.S. acknowledges support from NSF grants AST-1821967 and 1813708.

*Facility:* Magellan:Clay (Megacam).

*Software*: Astropy (Astropy Collaboration et al. 2013, 2018), The IDL Astronomy User's Library (Landsman 1993), DAOPHOT (Stetson 1987, 1994).

## ORCID iDs

Burçin Mutlu-Pakdil https://orcid.org/0000-0001-9649-4815
David J. Sand https://orcid.org/0000-0003-4102-380X
Denija Crnojević https://orcid.org/0000-0002-1763-4128
Alex Drlica-Wagner https://orcid.org/0000-0001-8251-933X
Nelson Caldwell https://orcid.org/0000-0003-2352-3202
Puragra Guhathakurta https://orcid.org/0000-0001-8867-4234
Anil C. Seth https://orcid.org/0000-0003-0248-5470
Joshua D. Simon https://orcid.org/0000-0002-4733-4994
Jay Strader https://orcid.org/0000-0002-1468-9668
Elisa Toloba https://orcid.org/0000-0001-6443-5570

## References

Abbott, T. M. C., Abdalla, F. B., Allam, S., et al. 2018, ApJS, 239, 18
Ahumada, R., Allende Prieto, C., Almeida, A., et al. 2020, ApJS, 249, 3
Akeson, R., Armus, L., Bachelet, E., et al. 2019, arXiv:1902.05569
Astropy Collaboration, Price-Whelan, A. M., Sipőcz, B. M., et al. 2018, AJ, 156, 123
Astropy Collaboration, Robitaille, T. P., Tollerud, E. J., et al. 2013, A&A, 558, A33
Bennet, P., Sand, D. J., Crnojević, D., et al. 2017, ApJ, 850, 109
Bennet, P., Sand, D. J., Crnojević, D., et al. 2019, ApJ, 885, 153
Bennet, P., Sand, D. J., Crnojević, D., et al. 2020, ApJL, 893, L9
Bennet, P., Sand, D. J., Zaritsky, D., et al. 2018, ApJL, 866, L11
Boulade, O., Charlot, X., Abbon, P., et al. 2003, Proc. SPIE, 4841, 72
Boylan-Kolchin, M., Bullock, J. S., & Kaplinghat, M. 2011, MNRAS, 415, L40
Boylan-Kolchin, M., Bullock, J. S., & Kaplinghat, M. 2012, MNRAS, 422, 1203
Bressan, A., Marigo, P., Girardi, L., et al. 2012, MNRAS, 427, 127
Brook, C. B., Di Cintio, A., Knebe, A., et al. 2014, ApJL, 784, L14
Brooks, A. M., Kuhlen, M., Zolotov, A., & Hooper, D. 2013, ApJ, 765, 22
Bryan, G. L., & Norman, M. L. 1998, ApJ, 495, 80
Bullock, J. S., & Boylan-Kolchin, M. 2017, ARA&A, 55, 343
Carlin, J. L., Garling, C. T., Peter, A. H. G., et al. 2019, ApJ, 886, 109
Carlin, J. L., Mutlu-Pakdil, B., Crnojević, D., et al. 2021, ApJ, 909, 211
Carlin, J. L., Sand, D. J., Price, P., et al. 2016, ApJL, 828, L5
Carlsten, S. G., Greene, J. E., Peter, A. H. G., Beaton, R. L., & Greco, J. P. 2021, ApJ, 908, 109
Cerny, W., Pace, A. B., Drlica-Wagner, A., et al. 2021, ApJ, 910, 18
Chiboucas, K., Jacobs, B. A., Tully, R. B., & Karachentsev, I. D. 2013, AJ, 146, 126
Chiboucas, K., Karachentsev, I. D., & Tully, R. B. 2009, AJ, 137, 3009
Crnojević, D., Sand, D. J., Bennet, P., et al. 2019, ApJ, 872, 80
Crnojević, D., Sand, D. J., Caldwell, N., et al. 2014, ApJL, 795, L35
Crnojević, D., Sand, D. J., Spekkens, K., et al. 2016, ApJ, 823, 19
Danieli, S., van Dokkum, P., Merritt, A., et al. 2017, ApJ, 837, 136
Davis, A. B., Nierenberg, A. M., Peter, A. H. G., et al. 2021, MNRAS, 500, 3854
Dickey, C. M., Geha, M., Wetzel, A., & El-Badry, K. 2019, ApJ, 884, 180
Dooley, G. A., Peter, A. H. G., Carlin, J. L., et al. 2017a, MNRAS, 472, 1060
Dooley, G. A., Peter, A. H. G., Yang, T., et al. 2017b, MNRAS, 471, 4894
Dotter, A., Chaboyer, B., Jevremović, D., et al. 2008, ApJS, 178, 89
Drlica-Wagner, A., Carlin, J. L., Nidever, D. L., et al. 2021, ApJS, 256, 2
Engler, C., Pillepich, A., Pasquali, A., et al. 2021, MNRAS, in press
Flaugher, B., Diehl, H. T., Honscheid, K., et al. 2015, AJ, 150, 150
Font, A. S., McCarthy, I. G., & Belokurov, V. 2021, MNRAS, 505, 783
Garrison-Kimmel, S., Wetzel, A., Bullock, J. S., et al. 2017, MNRAS, 471, 1709
Geha, M., Wechsler, R. H., Mao, Y.-Y., et al. 2017, ApJ, 847, 4
Greco, J. P., Greene, J. E., Strauss, M. A., et al. 2018, ApJ, 857, 104
Greco, J. P., van Dokkum, P., Danieli, S., Carlsten, S. G., & Conroy, C. 2021, ApJ, 908, 24
Hargis, J. R., Albers, S., Crnojević, D., et al. 2020, ApJ, 888, 31
Hughes, A. K., Sand, D. J., Seth, A., et al. 2021, ApJ, 914, 16
Ibata, R. A., Lewis, G. F., Conn, A. R., et al. 2013, Natur, 493, 62
Ivezić, Ž., Kahn, S. M., Tyson, J. A., et al. 2019, ApJ, 873, 111
Karachentsev, I. D., Makarov, D. I., & Kaisina, E. I. 2013, AJ, 145, 101
Karunakaran, A., Spekkens, K., Bennet, P., et al. 2020, AJ, 159, 37
Karunakaran, A., Spekkens, K., Oman, K. A., et al. 2021, ApJL, 916, L19
Klypin, A., Kravtsov, A. V., Valenzuela, O., & Prada, F. 1999, ApJ, 522, 82
Landsman, W. B. 1993, in ASP Conf. Ser. 52, Astronomical Data Analysis Software and Systems II, ed. R. J. Hanisch, R. J. V. Brissenden, & J. Barnes (San Francisco, CA: ASP), 246
Leisman, L., Haynes, M. P., Janowiecki, S., et al. 2017, ApJ, 842, 133
Mao, Y.-Y., Geha, M., Wechsler, R. H., et al. 2021, ApJ, 907, 85
Martin, N. F., de Jong, J. T. A., & Rix, H.-W. 2008, ApJ, 684, 1075
Martin, N. F., Ibata, R. A., McConnachie, A. W., et al. 2013, ApJ, 776, 80
Martin, N. F., McConnachie, A. W., Irwin, M., et al. 2009, ApJ, 705, 758
Martinez-Delgado, D., Karim, N., Boschin, W., et al. 2021, arXiv:2104.03859
Mau, S., Cerny, W., Pace, A. B., et al. 2020, ApJ, 890, 136
McLeod, B., Geary, J., Conroy, M., et al. 2015, PASP, 127, 366
Miyazaki, S., Komiyama, Y., Kawanomoto, S., et al. 2018, PASJ, 70, S1
Moore, B., Ghigna, S., Governato, F., et al. 1999, ApJL, 524, L19
Moster, B. P., Somerville, R. S., Maulbetsch, C., et al. 2010, ApJ, 710, 903
Müller, O., Ibata, R., Rejkuba, M., & Posti, L. 2019, A&A, 629, L2
Müller, O., Pawlowski, M. S., Jerjen, H., & Lelli, F. 2018, Sci, 359, 534
Muñoz, R. R., Côté, P., Santana, F. A., et al. 2018, ApJ, 860, 66
Munshi, F., Brooks, A. M., Christensen, C., et al. 2019, ApJ, 874, 40
Mutlu-Pakdil, B., Sand, D. J., Carlin, J. L., et al. 2018, ApJ, 863, 25
Nadler, E. O., Drlica-Wagner, A., Bechtol, K., et al. 2021, PhRvL, 126, 091101
Okamoto, S., Arimoto, N., Ferguson, A. M. N., et al. 2019, ApJ, 884, 128
Pawlowski, M. S., Pflamm-Altenburg, J., & Kroupa, P. 2012, MNRAS, 423, 1109

Putman, M. E., Zheng, Y., Price-Whelan, A. M., et al. 2021, ApJ, 913, 53
Rockosi, C. M., Odenkirchen, M., Grebel, E. K., et al. 2002, AJ, 124, 349
Samuel, J., Wetzel, A., Chapman, S., et al. 2021, MNRAS, 504, 1379
Sand, D. J., Crnojević, D., Bennet, P., et al. 2015b, ApJ, 806, 95
Sand, D. J., Crnojević, D., Strader, J., et al. 2014, ApJL, 793, L7
Sand, D. J., Olszewski, E. W., Willman, B., et al. 2009, ApJ, 704, 898
Sand, D. J., Spekkens, K., Crnojević, D., et al. 2015a, ApJL, 812, L13
Sand, D. J., Strader, J., Willman, B., et al. 2012, ApJ, 756, 79
Sawala, T., Frenk, C. S., Fattahi, A., et al. 2016, MNRAS, 457, 1931
Schlafly, E. F., & Finkbeiner, D. P. 2011, ApJ, 737, 103
Schlegel, D. J., Finkbeiner, D. P., & Davis, M. 1998, ApJ, 500, 525
Simon, J. D. 2019, ARA&A, 57, 375
Smercina, A., Bell, E. F., Price, P. A., et al. 2018, ApJ, 863, 152
Spekkens, K., Urbancic, N., Mason, B. S., Willman, B., & Aguirre, J. E. 2014, ApJL, 795, L5
Springel, V., Frenk, C. S., & White, S. D. M. 2006, Natur, 440, 1137
Stetson, P. B. 1987, PASP, 99, 191
Stetson, P. B. 1994, PASP, 106, 250
Tanaka, M., Chiba, M., & Komiyama, Y. 2017, ApJ, 842, 127
Tanoglidis, D., Drlica-Wagner, A., Wei, K., et al. 2021, ApJS, 252, 18
Tollerud, E. J., Geha, M. C., Grcevich, J., Putman, M. E., & Stern, D. 2015, ApJL, 798, L21
Toloba, E., Sand, D. J., Spekkens, K., et al. 2016, ApJL, 816, L5
Voggel, K. T., Seth, A. C., Sand, D. J., et al. 2020, ApJ, 899, 140
Walsh, S. M., Willman, B., & Jerjen, H. 2009, AJ, 137, 450
Weisz, D. R., Dalcanton, J. J., Williams, B. F., et al. 2011, ApJ, 739, 5
Wetzel, A. R., Hopkins, P. F., Kim, J.-h., et al. 2016, ApJL, 827, L23
Zaritsky, D., Donnerstein, R., Dey, A., et al. 2019, ApJS, 240, 1